

# Enhancement of High-Performance Graphene Biosensors for Cancer Detection

**Victor Pablo Acero**

**Engineering Science, The Pennsylvania State University**

**NNIN REU Site: Minnesota Nano Center, University of Minnesota-Twin Cities, Minneapolis, MN**

*NNIN REU Principal Investigator: Tianhong Cui, Mechanical Engineering, Tian Group, University of Minnesota-Twin Cities*

*NNIN REU Mentor: Shota Sando, Mechanical Engineering, Tian Group, University of Minnesota-Twin Cities*

*Contact: acero002@gmail.com, cuixx006@me.umn.edu, ssando@umn.edu*

## Abstract:

Current alpha-fetoprotein (AFP) sensing technologies such as enzyme-linked immunosorbent assays (ELISA) require a lot of equipment, time, and skill. Still, they would be less sensitive than our proposed graphene biosensors, which in theory could detect a single AFP. Graphene's unique material properties and sensitivity to the surrounding environment are exploited in our sensor for the detection of AFP. A U-shaped gold electrode containing a small gap for the sensing area would then be patterned using photolithography. The gap would be closed by covering the bare substrate with our few-layer-graphene (FLG) structure. We tune the thickness, and thus the properties, of graphene through a unique layer-by-layer self-assembly process that uses graphene solution and polyelectrolytes. The graphene sensing area is further prepared with poly-L-lysine and then functionalized with anti-AFP. Also, due to the fact that the ability to detect AFP is heavily limited by the signal-noise ratio, we redesigned the basic interface between gold and graphene in multiple ways to achieve a better signal-noise ratio in our sensors. The sensors that were fabricated were successful in detecting alpha-fetoprotein even in concentrations as low as 1 pg/ml. Lastly, the redesigned gold/graphene interface showed promising results and seems to have only been limited by our fabrication procedure.

## Introduction:

Graphene, the two-dimensional counterpart of graphite, has been extensively studied in terms of its properties and manufacturing since its discovery in 2004. Since its discovery a plethora of techniques have been developed for creating this new material [1]. Though popular methods produce quality graphene, they are not scalable to meet industry demand. However, this work uses layer-by-layer self-assembly to produce few-layer-graphene (FLG), which is indeed scalable.

This bio-sensor would be a candidate for phasing out and replacing the current bio-chemical assay known as ELISA, which is the industry standard for antigen screening. ELISA is a great tool, however it is complicated to screen antigens, it requires great technician skill, and takes hours to run. Conversely our sensor is simple to prepare for testing, the screening is simple, and data is visible in a matter of seconds/minutes.

We wanted to enhance our sensor sensitivity as well by reducing 1/f noise in our sensors. In order to do this we decided to try reducing the overall contact resistance present, thus we reduced the contact area between the graphene and gold [2,3].

## Methods and Techniques:

**Fabrication.** We fabricated our sensors using a photolithography process, as demonstrated in Figure 1, which involves the patterning of the gold electrode, patterning of graphene onto the sensing area, and the patterning of a protective KMPR coating.

**Modified Gold-Graphene Interface.** In order to reduce contact area between gold and graphene, the junction at which they meet was redesigned. This work used three different designs, as seen in Figure 2 — a 31 strip design, 95 strip designs, and 950 strip designs that reduced the

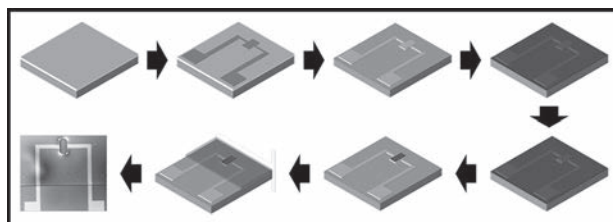


Figure 1: Process scheme.



Figure 2: The 31 strip design, 95 strip design, and 950 strip design.

surface area to 33%, 50%, and 50% respectively. The small feature size lead to occasional complications with fabrication, especially in the 950 strip design due to the 2 μm strip width.

**Graphene Self Assembly.** Next we facilitated the layer-by-layer self-assembly of few-layer-graphene onto the entire wafer. This was done by alternating immersion of the graphene wafer between a solution of poly(diallyldiamine chloride) (PDDA), which is positively charged, and poly(styrene sulfonate) (PSS), which is negatively charged; it enabled us to create a thin layer of polymer that distanced the graphene, once formed, away from the silicon oxide. Next we alternated immersion into PDDA and a solution of suspended negatively charged graphene platelets for five cycles to form FLG.

**Graphene Charge Sensitivity and Debye Length.** If there is a charge within the Debye length of the sensing area, the graphene's carrier mobility and resistance will be affected, however the affects vary depending on the charge present. Since graphene in our sensing area was P-doped, a negative charge within its Debye length would decrease resistance throughout the material, whilst contrariwise, a positive charge would increase the resistance in the graphene.

**Functionalization.** The sensing area was prepared in the following progression: immersion in poly-L-lysine, cleaned with distilled water, immersed in a solution of anti-alpha fetoprotein (anti-AFP), cleaned with Dulbecco's phosphate-buffered saline (DPBS), and finally immersed in diluted 1% bovine serum albumin (BSA).

**Results:**

**Alpha-Fetoprotein Sensing.** We allowed the sensor to calibrate when exposed to DPBS with no AFP and then began to slowly increase the concentration of AFP, as can be seen in Figure 3.

**Noise Reduction.** This approach of 1/f noise reduction by reduction of contact area between gold/graphene was successful. Though poor performance is seen in the 950 strip design, which can be attributed to poor fabrication of electrodes, the 95 strip and 31 strip designs had less 1/f noise than the original sensor design, as is seen in Figure 4. If applied to our sensors we would surely surpass sensitivity of tests such as ELISA.

**Future Work:**

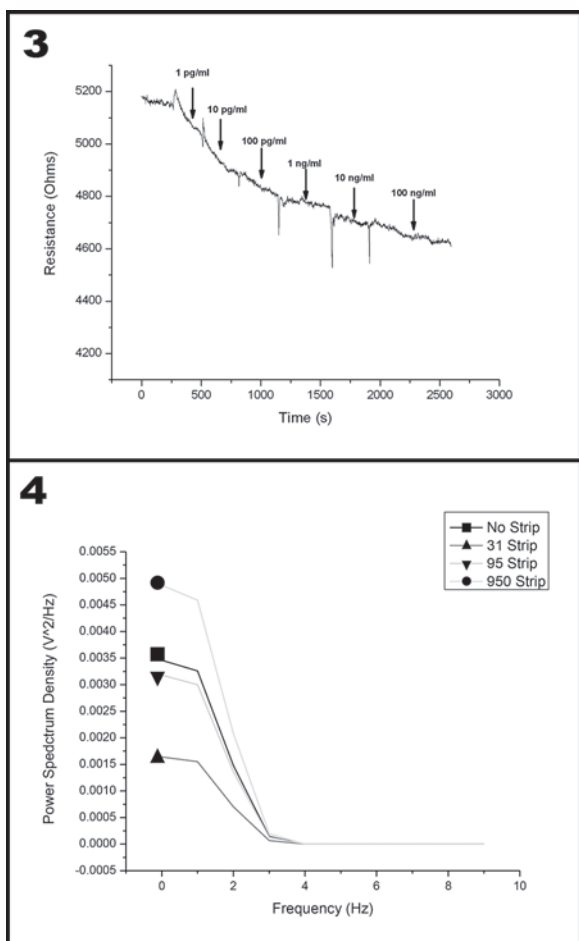
We would like to focus on two areas for future work. We would want to apply our work to flexible substrates to prove the potential application of our sensor as an *in vivo* bio-sensor, which is the consummation of our work. Lastly, we want to better understand the graphene-gold interface by finding the optimal value for contact area reduction and number of gold strips, in order to further improve the signal-to-noise ratio.

**Acknowledgments:**

I would like to acknowledge the TIAN lab at the University of Minnesota for their guidance and support, specifically Tianhong Cui and Shota Sando. I also want to thank the NSF and National Nanotechnology Infrastructure Network Research Experience for Undergraduates (NNIN REU) Program (Grant No. ECCS-0335765) for funding this research.

**References:**

- [1] Zhu, Y., Murali, S., Cai, W., (2010), Graphene and Graphene Oxide: Synthesis, Properties, and Applications. *Adv. Mater.*, 22: 3906-3924. doi:10.1002/adma.201001068.
- [2] Smith JT, Franklin AD. Reducing contact resistance in graphene devices through contact area patterning. *ACS Nano*, 7, 3661 (2013). <http://dx.doi.org/10.1021/nn400671z>.
- [3] Hyungwoo L. Wide Contact Structures for Low-Noise Nanochannel Devices Based on a Carbon Nanotube Network *ACS Nano* 2010 4 (12), 7612-7618 DOI: 10.1021/nn102296e.



# A PEDOT:PSS Process on Textiles for Health Monitoring

**Mariella Arias**

**Biomedical Engineering, El Camino College**

**NNIN iREU Site: Centre Microélectronique de Provence, École Nationale Supérieure des Mines de Saint-Étienne, France**

*NNIN iREU Principal Investigator: George Malliaras, Centre Microélectronique de Provence, École Nationale Supérieure des Mines de Saint-Étienne, France*

*NNIN iREU Mentors: Thomas Lonjaret and Esma Ismailova, Centre Microélectronique de Provence, École Nationale Supérieure des Mines de Saint-Étienne, France*

*Contact: ariasmariella.brm@gmail.com, malliaras@emse.fr, thomas.lonjaret@emse.fr, ismailova@emse.fr*

## Abstract:

Wearable electronic textiles are good candidates for achieving low cost, flexible, and light-weight health monitoring devices. The integration of biocompatible organic polymers, such as poly(3,4-ethylenedioxythiophene):polystyrene sulfonate (PEDOT:PSS), and ionic gels with textiles allows for the development of conformable and high performance electronics for cutaneous applications. For these reasons, we developed a fabrication process for PEDOT:PSS based electrodes. Such electrodes were used for recording electrocardiography (ECG) activity and for developing an electrochromatographic display of such activity. An ionic liquid gel was used to aid in the electrochemical doping and de-doping of the PEDOT:PSS electrodes. Color changes on the electrochromatographic display were analyzed via optical spectroscopy. The PEDOT:PSS electrodes were also used as capacitive pressure sensors, with polydimethylsiloxane (PDMS) as dielectric, for physiotherapeutic applications. Results obtained using this process pave the way for technology that can be further integrated on an electronic textile glove that can perform several health monitoring tasks at once.

## Introduction:

There is an increasing interest for combining the capabilities of electronics with textiles. This emerging field of research provides new tools for a variety of applications such as in the medical field. Detection of electrical activity of the heart by external electrodes, also referred to as electrocardiography (ECG), is a method used by physicians to investigate heart rhythm. This test can help physicians detect anomalies in the functions of the heart. To perform ECG testing, two or more metal electrodes are placed directly on top of skin. However, such metal electrodes can be expensive and, as they lack flexibility, do not conform well with skin. Having textile-based electrodes could allow for improved ECG testing as the flexibility of the textile enables to follow the movement of most human body parts. Furthermore, in this work we seek to expand the applications of textile-based electrodes to be used as capacitive sensors to detect changes in pressure. This technology can provide crucial information in the field of physiotherapy regarding pressure applied on patients.

in direct contact with skin. The textile electrodes were constructed by patterning the conductive polymer on polyester-based fabric. A negative polyimide master was used to define the desired pattern. On such master, a layer of PDMS was deposited by spin coating. The polyimide master was then placed on top of textile, with the PDMS in direct contact with the fabric (see Figure 1).

## Device Fabrication:

All materials used in this process are biocompatible, which allows for applications

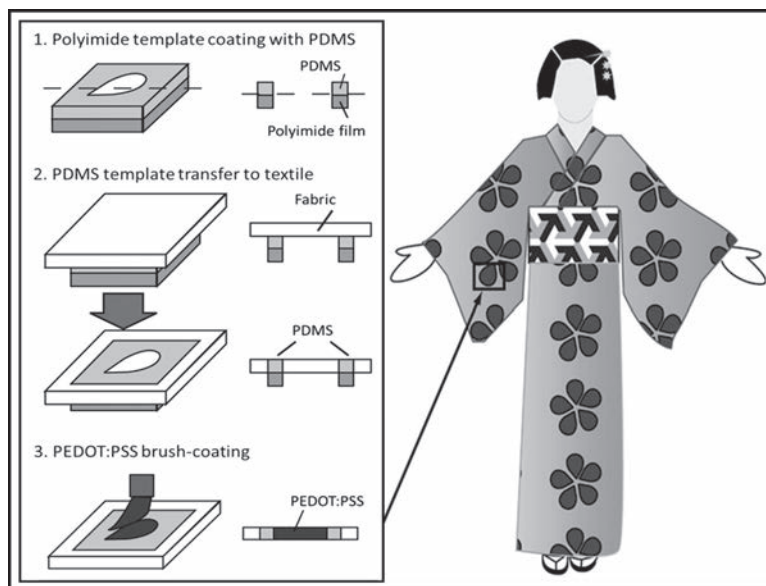
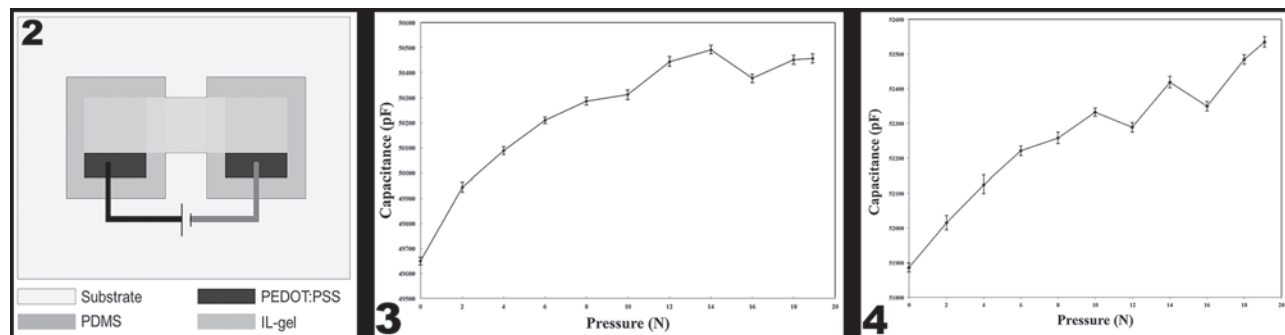


Figure 1: Patterning process.



**Figure 2, left:** Schematic of ECG display experimental setup. **Figure 3, middle:** Pressure sensing characterization. 920 μm thick PDMS layer as dielectric. **Figure 4, right:** Pressure sensing characterization. 560 μm thick PDMS layer as dielectric.

The PDMS was cured onto textile via thermal annealing for ten minutes at 100°C. The polyimide master was then removed from the PDMS surface. The hydrophobic properties of PDMS allowed for confinement of the PEDOT:PSS aqueous solution on textile substrate. Then, PEDOT:PSS solution was paint brushed on textile, and subsequently annealed for five hours at 100°C. The PEDOT:PSS solution was prepared in a 0.80/0.20/0.40/0.01 ratio of PEDOT:PSS aqueous dispersion, ethylene glycol, 4-dodecylbenzenesulfonic acid, and (3-glycidyoxypropyl) trimethoxysilane, respectively. Solution was then mixed, and sonicated for thirty minutes. The films were subsequently baked at 100°C for five hours.

### Experimental Procedure:

An ionic liquid gel was used aid in the electrochemical doping and de-doping of the PEDOT:PSS electrodes. The ionic gel consisted of the mixture of ionic liquid 1-ethyl-3-methylimidazolium-ethyl sulfate, 0.1M phosphate buffer solution, poly(ethylene glycol)diacrylate and the photoinitiator 2-hydroxy-2-8-methylpropiophenone at a ratio of 0.12/0.48/0.35/0.05, respectively. Two sets of experiments were arranged for testing the textile electrodes for two applications: electrodes as ECG-signal display, and electrodes as capacitive sensors. On this device, a sine wave of 100 mHz was applied, using potentials ranging from 0.2V to 2V (see Figure 2). This signal promoted ion migration between the electrodes. Because of the electrochromathographic properties of PEDOT:PSS, we observed changes in color with the naked eye alternating from light blue to dark blue. A glass slide was used as a substrate for the PEDOT:PSS electrodes.

The PEDOT:PSS electrodes were also used as capacitive pressure sensors, with polydimethylsiloxane (PDMS) as dielectric, for physiotherapeutic applications. The capacitor was formed by one layer PEDOT:PSS-textile electrode plates, and one of PDMS on top. The terminal of such textile electrode is connected to the circuit. The second conducting plate was a grounded metal electrode, to allow applied pressure variation. A range of pressures was applied to two capacitors with different dielectric thickness

(see Figures 3 and 4). Information regarding capacitance changes on device was obtained from the configuration of the setup of textile-PEDOT:PSS electrodes, capacitance measurement circuit in MCUs, and PC.

### Conclusion and Future Work:

We have successfully patterned textile electrodes for health monitoring practices using materials that are all biocompatible and inexpensive. Capacitance changes as a function of pressure were detected, varying with dielectric thickness, agreeing with theory. Textiles as capacitance sensors are promising for physiotherapy applications as we detected pressure changes in the range of 0.1N to 200N, which is the ideal range for such applications. ECG display process needs to be further investigated as the working frequency is not yet reaching 1 Hz, which is a normal ECG frequency. For this reason, we would like to investigate alternative ionic gels that will enable faster doping/de-doping response to match ECG signal frequency, and allow for transferring of process to textiles. Furthermore, future work will focus on optimizing patterning techniques to allow for further integration onto different shapes of substrates such as textile gloves.

### Acknowledgements:

This work was funded and supported by the National Nanotechnology Infrastructure Network International Research Experience for Undergraduates (NNIN iREU) Program and the National Science Foundation Grant No. ECCS-0335765, and was performed using the facilities at the Center of Microelectronics in Provence. I would like to thank the Department of Bioelectronics for their help and support.

### References:

- [1] G. D. Clifford, et al., "Advanced Methods and Tools for ECG Data Analysis", 1st Edition (2006). E-book.
- [2] S. Takamatsu, et al., "Meter-scale large-area capacitive pressure sensors with fabric with stripe electrodes of conductive polymer-coated fibers", *Microsystem Technologies*, March 2015.

# Tablet Analysis and Display of Semiconductor Biosensors

**Raymond Barakat**

**Electrical Engineering, Arizona State University**

**NNIN REU Site: Microelectronics Research Center, The University of Texas, Austin, TX**

*NNIN REU Principal Investigator: Prof. Ray Chen, Electrical and Computer Engineering, University of Texas at Austin*

*NNIN REU Mentor: Dr. Swapnajit Chakravarty, Omega Optics-Austin, Texas*

*Contact: rjbaraka@asu.edu, chen@ece.utexas.edu, swapnajit.chakravarty@omegaoptics.com*

## Abstract and Introduction:

Photonic crystals using silicon-on-insulator (SOI) processes have applications as extremely sensitive biosensors. By taking advantage of the photonic bandgap (PBG), light can be guided through the photonic crystal (PC) using PC micro-cavities to block light and PC waveguides to allow light through. When light shines through the PC biosensor, depending on the design, the output spectrum will display distinct resonances. When a sample is pipetted on the PC biosensor and a wavelength shift is observed. This shift can be used to determine what is in the sample and what its concentration is. Previous work has shown that PC biosensors have the capability to reliably detect biomarkers related to various cancers and dangerous elements in extremely low concentrations.

The goal of this project is to develop software in MATLAB that quickly collects and analyzes spectrum data received from the biosensor. The software is also able to control a near-infrared SLED light source in order to perform repeated scans and analyses on data collected from an optical spectrum analyzer (OSA). This software will run on a tablet in order to explore the feasibility of a portable biosensing platform. Tests were performed on a biosensor using the 2A81G5 antibody as a probe in order to detect cadmium ions in solution. Current work is being done to refine the software suite developed, such as improving the accuracy of resonance detection and tracking. This will make data collection easier so the biosensor will be more practical to use.

## Experimental Procedure:

To collect data from the PC biosensor the following tools were used: an OSA with USB connectivity, a near-infrared SLED source, and MATLAB software loaded onto a Surface Pro 2 tablet. MATLAB code was written to interface with the OSA and the SLED source. Further code was written to analyze the collected data and plot the results in a graphical user interface (Figure 1). The *findpeaks()* MATLAB function was used to find and initially plot all the local minima to approximate the location of multiple resonances (Figure 2). Next the *smooth()* function was used to smooth noisy spectrum data from the OSA using a moving average (Figure 3). Finally, *lorentzfit()* was used to fit a Lorentzian curve to the smoothed data using a least squares approximation, and *mins()* was used to find the final location of the resonance wavelength (Figure 2) [1]. All of this functionality was controlled using the MATLAB GUI. For the repeated scans of the biosensor the Surface Pro 2 was connected to the OSA and optical fibers were connected between the OSA, positioning stage, and the SLED. The biosensor was then placed and aligned on the positioning stage and a sample solution was pipetted onto the sensor. Next the user configured the SLED, OSA, and scan time using the GUI. A timer appeared while the scans were in progress, while the spectrum data and the detected minima were plotted and saved in real time. The user could stop the scans or reset the GUI using the onscreen buttons. The CSV files of the spectrum and minima data were saved in a folder for future analysis.

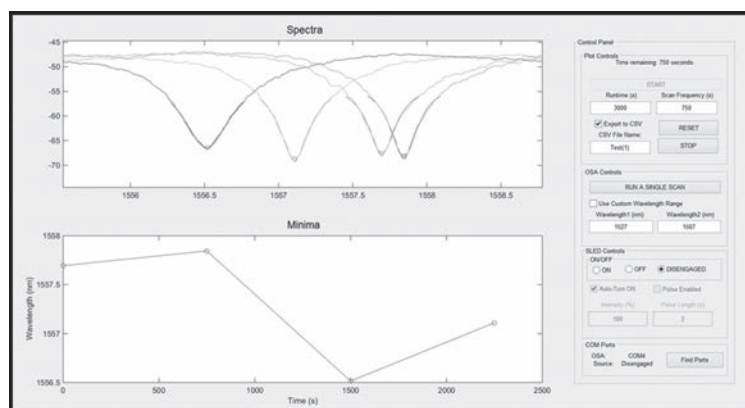


Figure 1: MATLAB GUI performing real time scans and tracking the chosen resonance's wavelength shift.

## Results:

Tests were performed using samples such as DI-water, glycerol, glutaraldehyde, BSA with and without probe proteins, and cadmium-ion solution. The sensor preparation is described in Reference 2, Part C. Preliminary tests were done using an L13 comparing the wavelength shift between water and glycerol to calibrate the OSA and test the minimum detection software. Subsequent tests were also done using an L13 biosensor conditioned using established methods from the lab group's previous work [2]. The wavelength shift observed in the most successful (Figure

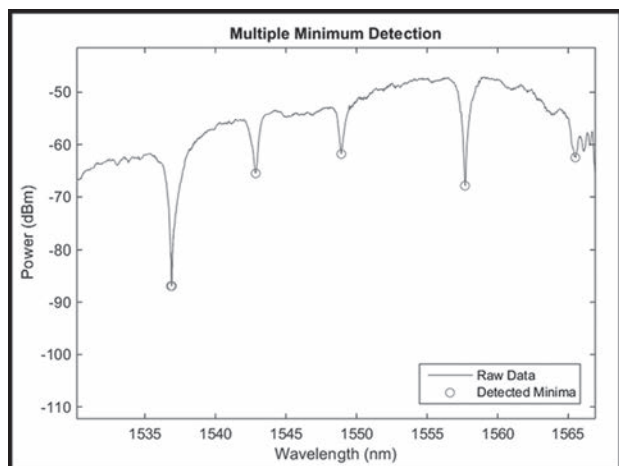


Figure 2: Example of multiple minima being detected by MATLAB.

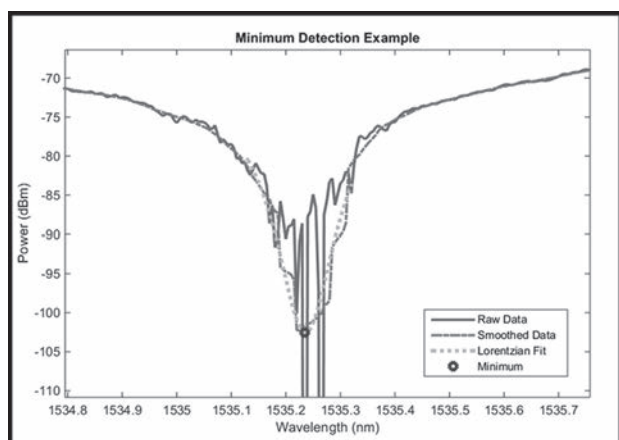


Figure 3: MATLAB smoothing raw data and fitting a Lorentzian curve to find a more accurate minimum.

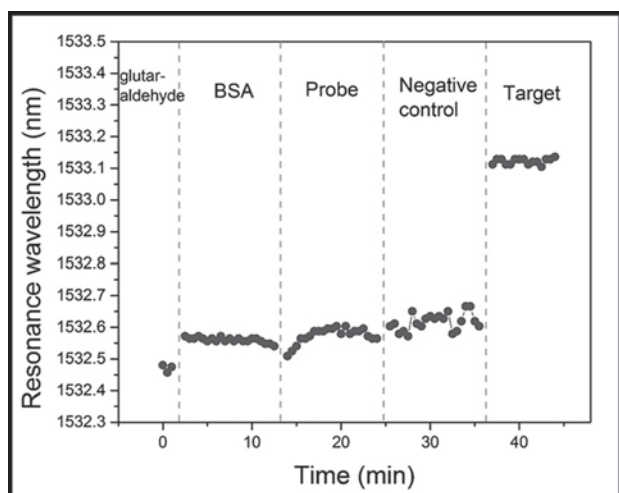


Figure 4: Data from an L13 biosensor during a repeated scan test where a resonance wavelength shift can be observed.

4) matches expected values of about a 0.5 nm wavelength shift for about 50 ppm cadmium-ions in solution.

### Conclusions:

The software developed performs at a level equal to or better than manual analysis. Biosensor behavior is more easily characterized in response to different samples in solution. More work on this software will make PC biosensors more practical sensor for use in real-world applications. Future work includes automating sample placement over the sensor using microfluidics and specialized pumps [3]. The biosensors could potentially be used to detect many different materials with more complete characterization data. These advances will allow more widespread use of PC biosensors and more accurate detection of materials in solution.

### Acknowledgements:

I would like to thank Dr. Swapnajt Chakravarti and Professor Ray Chen for their expertise. Thanks to Melvin Gutierrez for his work on the GUI and the SLED software and to Peter Grubb for his guidance on the project. Also, thanks to Hai Yan and Yi Zou for their help setting up the PC biosensor for testing. Finally, thanks to both the National Nanotechnology Infrastructure Network Research Experience for Undergraduates (NNIN REU) Program and the National Science Foundation (NSF) for providing this research opportunity under Grant No. ECCS-0335765.

### References:

- [1] lorentzfit(x,y,varargin) by Jered Wells, MATLAB File Exchange, August 3, 2015.
- [2] Zou, Y.; Chakravarty, S.; Chen, R.; et al.; "Waveguide Coupling Engineered High Sensitivity Silicon Photonic Crystal Microcavity Biosensors With High Yield"; IEEE Journal of Selected Topics in Quantum Electronics, 20, 4 (2014).
- [3] Wang, Z.; Yan, H.; Chakravarty, S.; Chen, R.; et al.; "Microfluidic channels with ultralow-loss waveguide crossings for various chip-integrated photonic sensors"; OPTICS LETTERS, 40, Page 1563-1566 (2015).

# Synergistic Effect of Adhesive Ligand Density and Soluble Factor TGF- $\beta$ on Epithelial Mesenchymal Transition Progression

Allison Bosworth

Biological Engineering, Louisiana State University

NNIN iREU Site: National Institute for Materials Science (NIMS), Tsukuba, Ibaraki, Japan

NNIN iREU Principal Investigator: Prof. Jun Nakanishi, International Center for Materials Nanoarchitectonics (MANA), National Institute of Materials Science (NIMS), Tsukuba, Japan

NNIN iREU Mentor: Dr. Saw Marlar, International Center for Materials Nanoarchitectonics (MANA), NIMS, Tsukuba, Japan

Contact: allison.bosworth1@gmail.com, nakanishi.jun@nims.go.jp

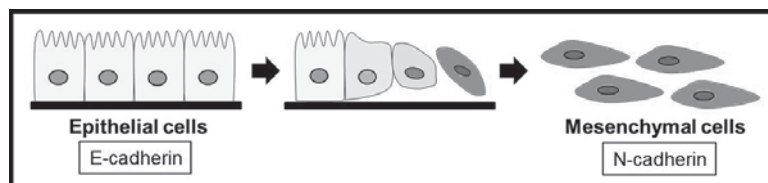


Figure 1: Visual schematic of EMT progression.

## Introduction:

Characterized by a change in cellular phenotype and an adjustment in protein expression, the epithelial mesenchymal transition (EMT) describes the transformation of epithelial cells into a mesenchymal cell type. This transition is involved in the initial stages of cancer metastasis and enhances the migratory capacities and evasiveness of cancer cells [1]. In this study, we investigated the impact of two factors—surface density of an extracellular matrix protein-derived ligand and soluble transforming growth factor- $\beta$ 1 (TGF- $\beta$ 1)—on the progression of EMT. Gold surfaces functionalized in various ratios of adhesive ligand cRGD to bio-inert ethylene glycol (EG) were seeded with epithelial cells. This technique allows for simultaneous comparison of different stages of EMT in which morphological differences and changes in protein expression can be recorded. By investigating EMT in smaller, discrete steps, we can more accurately analyze the underlying mechanisms that drive this transformation and that ultimately drive cancer metastasis. For these experiments, Madine-Darby canine kidney (MDCK) cells were used.

## Materials and Methods:

To study EMT progression, a five-day procedure was employed. On day one, gold (Au)  $5 \times 5 \text{ mm}^2$  surfaces were cleaned via sonication in acetone and UV-ozone treatment. The bare Au surfaces were then coated with various concentrations of cyclic [Arg-Gly-Asp-D-Phe-Lys], or cRGD, in EG overnight.

Figure 2 illustrates the structure of cRGD, represented by L, alongside EG bound to a Au surface. Because cRGD binds to  $\alpha_v\beta_3$ -integrin receptors on the MDCK cell membrane,

it renders the Au surface adhesive to MDCK cells. Since EG repels protein absorption, MDCK cells attach to the surface exclusively by integrin binding to surface cRGD peptides. Adjusting the mixing ratio of adhesive ligand cRGD to protein-repellent ligand EG on the surface allows for effective tuning of surface adhesiveness to cells. Two mixing ratios of cRGD:EG were used in these experiments—1:100 (100 $\times$ ) and 1:10,000 (10k); 100 $\times$  represents a high-density cRGD surface, while 10k represents a low-density cRGD surface.

On day two, approximately  $5 \times 10^4$  MDCK cells per  $10 \text{ cm}^2$  were seeded onto each of the cRGD-coated surfaces in serum-free medium to preempt any unwanted interaction of serum proteins with cell attachment at the beginning. Three hours after initial cell seeding, serum-free medium was aspirated and replaced with complete medium. On the following day, complete medium was supplemented with TGF- $\beta$  at 10 ng/mL to induce EMT in two of the four samples. After two days of incubation with adhesive ligand cRGD and soluble growth factor TGF- $\beta$ , MDCK

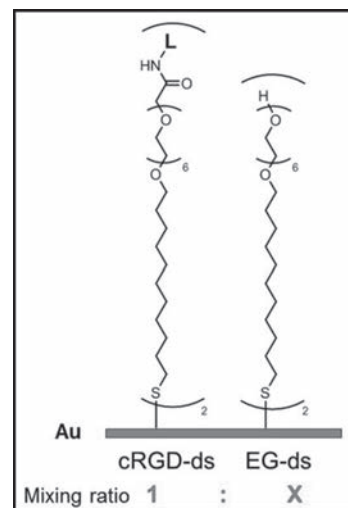


Figure 2: Surface self-assembled monolayers on a gold surface with “L” representing cRGD.

cells were fixed to the gold surfaces with a 1:1 methanol:acetone solution. From there, primary antibodies bound to membrane proteins E-cadherin and N-cadherin. Fluorescently-tagged secondary antibodies then bound to the primary antibodies. These secondary antibodies fluoresce upon exposure to UV light to aid in visualization of membrane proteins. This process of immunofluorescent staining was utilized to study the presence of cadherin proteins in MDCK cells on day five. Localization of E-cadherin or N-cadherin to the MDCK membrane indicates an epithelial or mesenchymal phenotype, respectively.

### Results and Discussion:

Both the adhesive ligand cRGD, and the soluble factor, TGF- $\beta$ , played a role in controlling EMT progression in MDCK cells. Figures 3 and 4 show EMT progression from left to right with a decrease in cRGD concentration from 100 $\times$  to 10k and with the addition of TGF- $\beta$ . At high cRGD densities and no TGF- $\beta$ , cells form tight clusters with a localization of F-actin in the cortical region of the cells. As cRGD density is decreased and TGF- $\beta$  is added, cells begin to elongate, move away from the tightly-bound clusters, and organize F-actin into intracellular fibers. Finally at low cRGD and the presence of TGF- $\beta$ , cells are completely elongated and F-actin is almost completely intracellular. This elongation and migration of cells coupled with the reorganization of actin within the cells allowed us to evaluate the EMT progression into four discrete steps.

To confirm this interpretation, protein localization of E-cadherin, an epithelial marker, and N-cadherin, a mesenchymal marker, was compared. At high cRGD densities and no TGF- $\beta$ , cells localized E-cadherin proteins to the membrane while at low cRGD densities and the presence of TGF- $\beta$ , cells localized N-cadherin to the cell membrane. Membrane localization of E-cadherin was less apparent than localization of N-cadherin perhaps because cells on 100 $\times$  surfaces formed tight aggregates. Moreover, these trends in protein localization to the membrane support the conclusion that EMT progression was separated into four discrete steps.

### Conclusions:

Lowering cRGD surface density and adding TGF- $\beta$  gives a controlled progression of EMT in MDCK cells. Adjusting

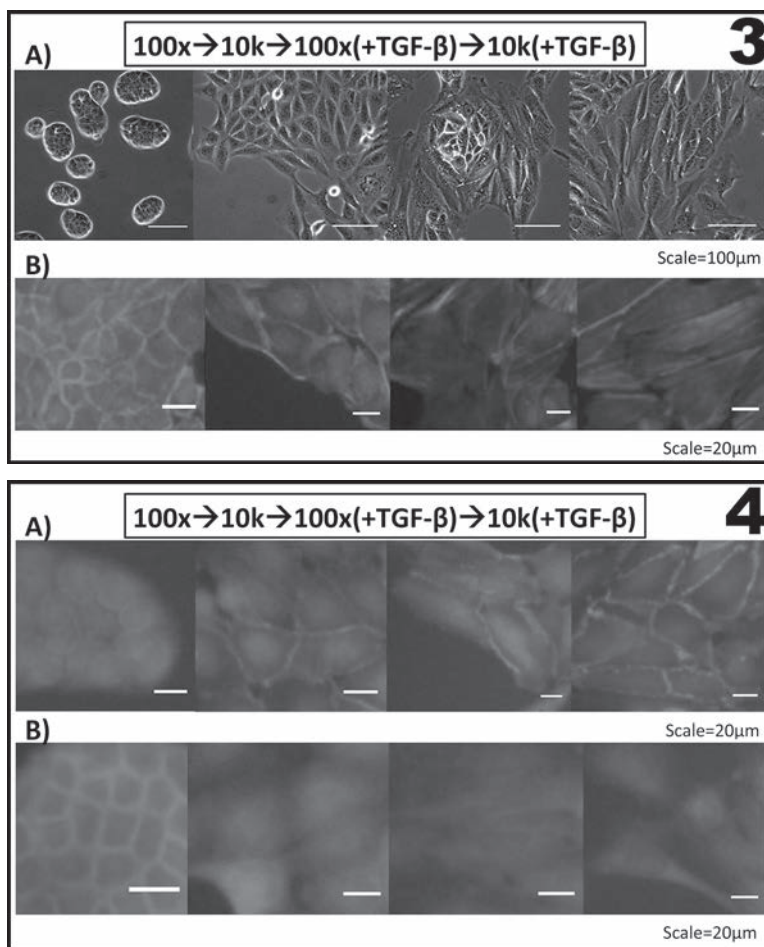


**Figure 3**, top: (A) Phase contrast images at day five. (B) Actin stained MDCK cells at day five. **Figure 4**, bottom: (A) N-cadherin and (B) E-cadherin stained MDCK cells at day five.

the concentration of TGF- $\beta$  and surface density of cRGD allows for analysis of underlying mechanisms at various degrees of EMT progression, which may give rise to novel metastatic therapeutic techniques. Future work for this project includes the quantification of gene expression via PCR or western blot to determine specifically the degree of EMT progression of each sample.

### Acknowledgments:

Funding for this project was provided by the National Science Foundation under Grant No. ECCS-0335765. Special thanks to National Nanotechnology Infrastructure Network International Research Experience for Undergraduates (NNIN iREU) Program coordinators and members of the Nakanishi lab group at the National Institute for Materials Science in Tsukuba, Japan.

### References:

- [1] Kalluri, Raghu, et al. J. Clinical Invest., 119, 6, 1420-1428 (2009).

# Fully Printed Organic Electrochemical Transistor on Paper for Glucose Sensing

Christopher Davidson

Biological Systems Engineering, University of Nebraska-Lincoln

**NNIN iREU Site: Centre Microélectronique de Provence, École Nationale Supérieure des Mines de Saint-Étienne, France**

NNIN iREU Principal Investigator: Dr. George Malliaras, Department of Bioelectronics, École Nationale Supérieure des Mines de Saint-Étienne

NNIN iREU Mentor: Eloïse Bihar, Department of Bioelectronics, École Nationale Supérieure des Mines de Saint-Étienne

Contact: cdavidson222@gmail.com, malliaras@emse.fr, bihar@emse.fr

## Abstract:

Inkjet printing of conductive polymers is a versatile, low-cost, and non-contact fabrication method for bioelectronic devices. In this study, an all-plastic glucose biosensor based on an organic electrochemical transistor (OECT) was printed on a paper substrate. An aqueous bioelectronic ink consisting of the conductive polymer poly(3,4-ethylenedioxythiophene)-poly(styrene sulfonic acid) (PEDOT:PSS) was used to print the source, drain, channel, and gate of the transistor. An ink containing chitosan/ferrocene solution was also printed to functionalize the PEDOT:PSS gate. Bioenzymatic sensing of glucose was then completed with these devices by using glucose oxidase (GOx) and phosphate buffered saline (PBS) as the enzyme and electrolyte, respectively. Initial results show glucose detection between 2.70 and 10.00 millimolar, consistent with the concentration in human blood. These results pave the way to establishing a simple, low-cost, and paper based biosensing platform suitable for point of care diagnostics.

## Introduction:

OECTs have recently gained great attention due to their high biocompatibility, ease of fabrication, and operation in low voltages, making them ideal candidates for bioelectronic applications. PEDOT:PSS is a conductive polymer ideal for fabricating OECTs due to its high conductivity, commercial availability, and its exceptional film forming properties [1]. In this study, we focused on inkjet printing a glucose sensing device. Inkjet printing is an ideal fabrication process as it presents advantages such as speed, flexibility, and low cost [2]. It can also successfully print on a multitude of substrates, including paper. Paper is an ideal substrate, as it is eco-friendly, disposable, and very inexpensive.

In this work, glucose is detected by inducing the enzyme specific reaction of glucose and GOx coupled with ferrocene, as shown in Figure 1. Ferrocene acts as an electron shuttle from the GOx to the PEDOT:PSS gate, causing de-doping of the channel and thus decreasing the drain current. This decrease is proportional to the concentration of glucose in the working solution [3].

## Experimental Procedure:

A Dimatix Materials Printer (DMP) was used to print the device, and its dimensions are shown in Figure 2. The channel and gate dimensions (length and width) were 5 mm × 1 mm and 5 mm × 2 mm, respectively. We printed

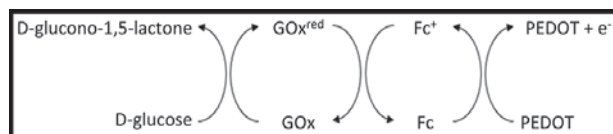


Figure 1: Reaction cycle for glucose detection using a ferrocene mediator.

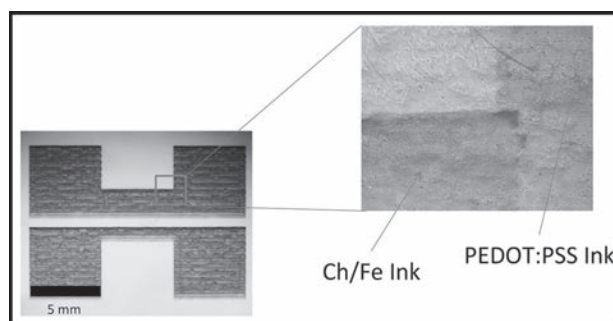


Figure 2: Fully printed OECT with zoom on gate.

two layers of pre-developed PEDOT:PSS ink recipe to fabricate the channel, drain, source, and gate of the transistor.

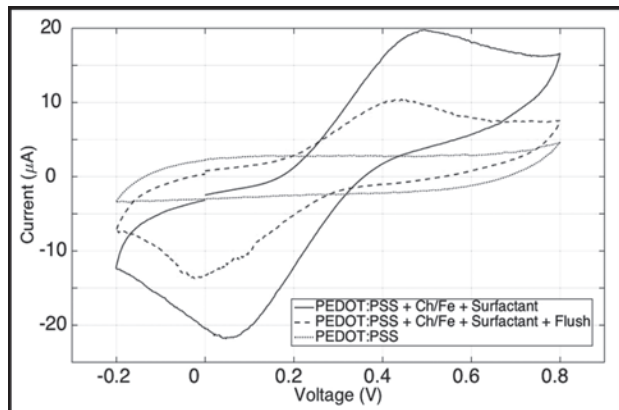


Figure 3: Cyclic voltammograms for different chitosan/ferrocene inks compared to PEDOT:PSS.

To make the electron mediator ink, a chitosan/ferrocene solution in acetic acid (0.3%wt) was first made by dissolving 15 mg of chitosan/ferrocene copolymer in 5 mL of 0.2 M acetic acid. To match this solution with the requirements of inkjet (rheological properties of the ink), we added a surfactant (Dynol 810) and a flush solution (water and ethylene glycol).

To assess the electrochemical performance of the ink in each step of its development, cyclic voltammetry was employed using a platinum wire as counter electrode, an Ag/AgCl reference electrode, and our ink as the working electrode, and can be seen in Figure 3.

Electrical characterization of the printed devices was carried out at a constant gate voltage of 0.5 V and a drain voltage of -0.7 V. In order to confine the electrolyte, a polydimethylsiloxane (PDMS) well was placed on top of the gate and channel, and the electrolyte (16  $\mu$ L) and the enzyme (2  $\mu$ L) were added. After stabilization of the drain current, different concentrations of glucose solutions were added. Figure 4 shows the device response to incremental steps in glucose concentration.

### Results and Conclusion:

Figure 3 shows the cyclic voltammograms of the chitosan/ferrocene ink after addition of surfactant, after further addition of flush solution, and a control of PEDOT:PSS. Peaks can be observed at around 0.4 V and 0.1 V for both inks containing chitosan/ferrocene solution, confirming the electrochemical activity of ferrocene.

Figure 2 shows a fully printed device. There is a clear color change between the gate and the rest of the device, indicating that the chitosan/ferrocene ink was selectively printed onto the gate of the device.

Figure 4 shows the device response upon successive additions of different glucose concentrations onto the device. There are clear changes in the current values for

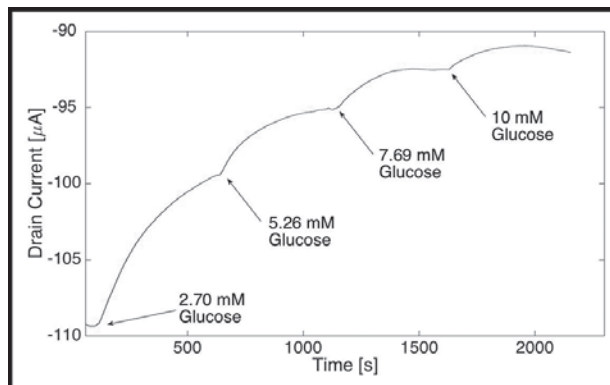


Figure 4: Device response to 2.70, 5.26, 7.69, and 10.00 mM glucose concentrations.

a range of concentrations between 2.70 mM and 10 mM, which are consistent with those in human blood [4].

### Conclusions and Future Work:

In this study, PEDOT:PSS and chitosan/ferrocene based inks were successfully printed on paper towards the development of an all printed paper OECT based glucose sensor. The detection of glucose was successful in a range of concentrations between 2.70 and 10.00 mM, similar to that in human blood. There is room for optimization, like immobilizing the enzyme on the gate and improving the sensor's sensitivity to the  $\mu$ M range, which is consistent with levels in human saliva. This work shows great potential as a disposable noninvasive sensing platform for point of care diagnostics.

### Acknowledgments:

I would like to thank the NNIN iREU Program and NSF for funding this project (under Grant No. ECCS-0335765). I would also like to thank Eloïse Bihar, Anna-Maria Pappa, Xenofon Strakosas, Mary Donahue, Vincenzo Curto, and Dr. George Malliaras for their individual help and guidance.

### References:

- [1] Shim, N, et al. All-Plastic Electrochemical Transistor for Glucose Sensing Using a Ferrocene Mediator. *Sensors* 2009;9:9896-9902.
- [2] Yun, YH, et al. A Glucose Sensor Fabricated by Piezoelectric Inkjet Printing of Conducting Polymers and Bionzymes. *Anal. Sci.* 2011;27:375-379.
- [3] Strakosas X, Bongo M, Owens RM. The organic electrochemical transistor for biological applications. *J. Appl. Polym. Sci.* 2015;132:41735.
- [4] Panchbhai, AS, et al. Correlation of Salivary Glucose Level with Blood Glucose Level in Diabetes Mellitus. *J. Oral. Maxillofac. Res.* 2012;3(3):e3.

# Imaging Live DU145 Cancer Cells Using Scanning Probe Microscope

Catherine Demos

Bioengineering, Clemson University

**NNIN REU Site: Howard Nanoscale Science and Engineering Facility, Howard University, Washington, DC**

*NNIN REU Principal Investigator: Dr. Tina Brower-Thomas, College of Engineering Architecture and Computer Science, Howard University*

*NNIN REU Mentor: Dr. Paulette Furbert-Harris, Cancer Center, Howard University Hospital*

Contact: [cdemos@clemson.edu](mailto:cdemos@clemson.edu), [tina.browerthomas@howard.edu](mailto:tina.browerthomas@howard.edu), [pfurbert-harris@howard.edu](mailto:pfurbert-harris@howard.edu)

## Abstract:

Different body cells have unique surface proteins that conduct electricity. Cell electrophysiology is the key to differentiating cancerous cells from healthy cells *in vivo*. Silicon carbide (SiC) is a biocompatible, chemically inert, thermally stable material on which we have tested the viability of DU145 cells. Using highly doped SiC, the relative conductivity of cells can be detected via current-sensing atomic force microscopy (CSAFM) with a flow cell to examine the living DU145 cells in media. A parallel part of this experiment is to functionalize the SiC surface to achieve specificity when attaching cells to confirm that the CSAFM method of identification is successful. After cleaning, an oxide layer is formed on the surface, then 3-aminopropyltriethoxysilane (APTES) is attached to result in a surface amenable to protein attachment followed by antibody attachment, which is the key to binding specific cells in specific areas of the substrate.

## Introduction:

SiC possesses properties that make it an ideal substrate for a new method of detection and treatment. This experimental method relies on the ability to identifying different types of cells based on the electrical signatures of the membranes from a unique combination of surface proteins, ion channels, and membrane potentials [1].

## Experimental Procedure:

All experiments were performed with commercially purchased 6H highly doped SiC. All samples were ultra-sonicated for three minutes each in methylene chloride, acetone, and isopropanol, sequentially. Next they were submerged in a 5:1:1 mixture of deionized (DI) water, H<sub>2</sub>O<sub>2</sub>, and NH<sub>4</sub>OH at 80°C for 10 minutes, which is the standard RCA cleaning procedure.

Two methods of oxidation and further cleaning were used to increase the reactivity of the SiC surface. One was oxygen plasma etching using a Plasma-Therm model 790 plasma enhanced system using a 20% oxygen/80% argon gas mixture for one and five minutes. The other was a tube furnace at 1000°C for 10, 30, and 60 minutes, with oxygen flowing for the duration of the heating period and argon as the samples cooled. After a thin oxide layer developed on the SiC, the samples were left exposed to air for three hours to ensure surface chemisorption of water molecules and increase the ability of the SiC to hydrolyze APTES in the next stage.

APTES silonization was performed in a class 100 clean room in an anhydrous N<sub>2</sub> environment. The samples

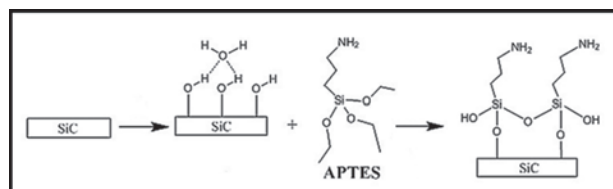


Figure 1: The APTES reaction with SiC.

were placed in a 1:49 solution of APTES in toluene for a duration of 30 minutes. They were then ultra-sonicated in toluene for 10 minutes and isopropanol for one minute, then dried under a stream of N<sub>2</sub> gas to remove any loose APTES molecules [2]. The steps are illustrated in Figure 1.

Additionally, DU145 prostate cancer cells were tested for viability on SiC. Cells were combined with RPMI media and the concentration was adjusted to  $5 \times 10^4$  cells/ml—the optimal seeding count determined in previous experiments. SiC was placed in a sterile 6-well culture plate, some carbon-face up, others silicon-face up; 2 ml of the cells were added to each well and incubated overnight at 37°C at 5% CO<sub>2</sub>. Inverted light microscopy was used to confirm binding of cells to the substrate. Two plates were used for sizing, with the cells on the substrates measured after 24 hours, and another two examined viability of the cells for an extended growing period of eight days, one checked every 24 hours and one left undisturbed.

CSAFM is the method used to evaluate the electrophysiological properties of the DU145 cells once they were bound to a substrate. The goal was to examine

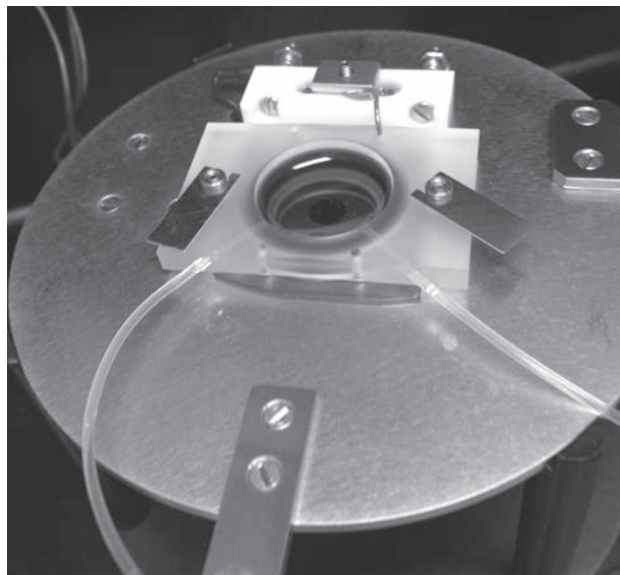


Figure 2: Flow cell and sample in media.

living cells, so a method of keeping them in fresh media while being scanned was necessary. We constructed a pump system with a flow cell for Agilent Technologies 5500 AFM shown in Figure 2 to allow media to flow in and overflow to be drawn out of the sealed area containing the sample. This allowed the cells to be scanned while living for about six hours out of the incubator and sterile environment.

### Results and Conclusions:

The carbon-face samples grew the most and the largest cells, though both carbon- and silicon-face samples did as well as or better than the control well in cell attachment after 24 hours. Images of this experiment are found in Figure 3. These findings confirm previous experiments done by this lab.

For CSAFM, it was found that when the cells were left for at least six days in undisturbed incubation, they were attached enough to probe with the tip of the AFM and examine topographically. Before that time, the cells were either not confluent enough or not attached strongly enough to remain in place when probed with the tip of the sensor. In Figure 4 are some of the first topographical images

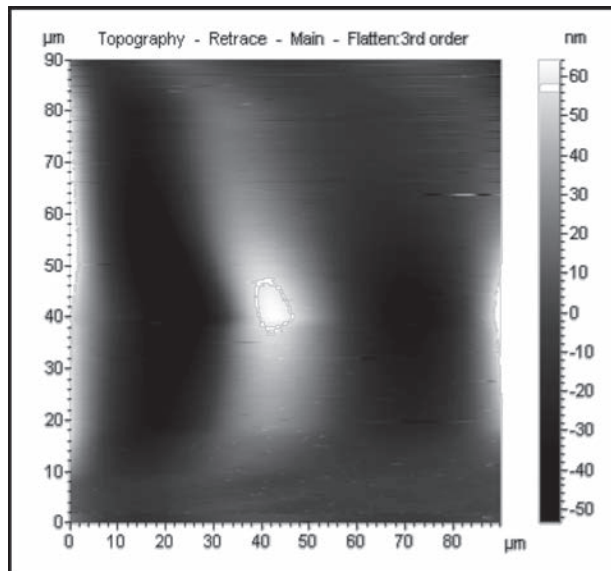


Figure 4: A topographical AFM image of a fibroblast.

obtained. The current-voltage part of the examination was not completed, as the media was too ionic to obtain accurate electrical profiles of the cells themselves. This is being addressed by our lab's collaborators.

### Future Work:

In the future, the method of functionalization needs to be confirmed and taken further with the attachment of Protein A and IgG antibodies. This will allow for specific attachment of cells in predetermined locations, so the AFM can be confirmed as a valid method of identification. Also, the cells need to be more strongly adhered to the surface of the SiC so the AFM tip does not remove them during scanning. A different media or additive may help with creating more junctions for cell attachment.

### Acknowledgements:

Thank you to Dr. Tina Brower-Thomas, Dr. Paulette Furburt-Harris and the staff of the Howard Nanoscale Facility for their guidance, the NNIN REU Program for the opportunity and the NFS for funding the project under Grant No. ECCS-0335765.

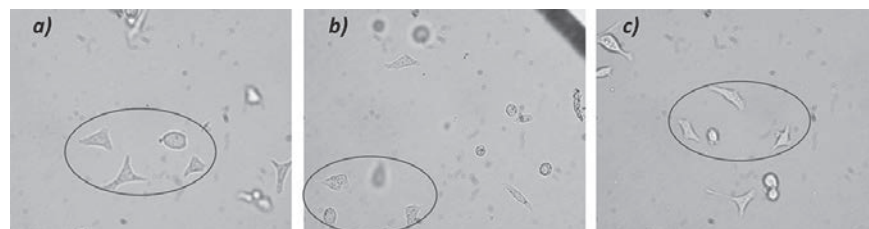


Figure 3: a) Carbon-face. b) Silicon-face. c) Control (empty well). Images taken at 24 hours (20x 1.6x).

### References:

- [1] Rzany A, Schaldach M. Progress in Biomedical Research. 2001; 6: 182-194.
- [2] Williams, E., et al. Applied Surface Science. 258, (16), 6056-6063 (2012).

# Exploration of Protein Capture Methods for Applications in Microfluidic Devices

**Matthew Devlin**

**Biomedical Engineering, Georgia Institute of Technology**

**NNIN REU Site: Cornell NanoScale Science and Technology Facility, Cornell University, Ithaca, NY**

*NNIN REU Principal Investigator: Haiyuan Yu, Weill Institute for Cell and Molecular Biology,  
Department of Biological Statistics and Computational Biology, Cornell University*

*NNIN REU Mentor: Robert Fragoza, Weill Institute for Cell and Molecular Biology,  
Department of Molecular Biology and Genetics, Cornell University*

*Contact: mrdevlin@gatech.edu, haiyuan.yu@cornell.edu, rf362@cornell.edu*

## **Abstract:**

On-chip protein immunoprecipitation is often a substantial limitation in the continued development of microfluidic tools for detecting protein-protein interactions in high throughput. Though adaptable surface chemistry on glass and polydimethylsiloxane (PDMS) lend themselves to robust, on-chip protein immobilization, problems such as non-specific protein adsorption, rigorous washing conditions, and low protein synthesis yields readily diminish assay sensitivity in protein interaction screens. In an effort to improve on-chip protein expression levels, we explored various chip-protein conjugation methods, including antibody crosslinking via (3-aminopropyl)triethoxysilane-derivatized (APTES) surfaces, Protein A-conjugated surfaces, as well as streptavidin-biotin coated surfaces. Increasing sensitivity to expressed protein was also explored through varying concentrations of both capture and probe antibodies as well as through the adjustment of enzyme-conjugated or fluorescently-labeled probe antibodies. Through our protein-surface conjugation experiments, we are able to successfully synthesize and capture protein on-chip. Continued development towards quantifying the binding strengths of protein-protein interactions would mark a substantial advancement in cellular proteomics and may also help unveil new drug targets in human disease.

## **Introduction:**

A longstanding goal in biological research has been to fully uncover the function of proteins encoded by human genomes as well as how their expression is regulated. Consequently, researchers have been working adamantly towards the development of high-throughput systems for expressing proteins and detecting their interactions under the paradigm that the function of a protein can be better understood by knowing who its interaction partners are. Though many well characterized high-throughput methodologies for detecting protein-protein interactions exist, including yeast two-hybrid and nucleic acid programmable protein array, these methods often suffer from limited specificity and high expense [1].

Microfluidic approaches such as Protein Interaction Network Generator demonstrate promise towards improving specificity and throughput but, due to difficulties in expressing and isolating human proteins through cell-free expression systems, have not been used to screen for human protein interactions on a large scale — a gap we aim to address [2]. The ability to quantify and generate protein-protein interactions networks could, in consequence, improve our understanding of how human disease alters cell signaling networks and potentially unveil new pharmaceutical drug targets.

## **Experimental Procedure:**

Glass microscope slides underwent an oxygen plasma treatment before a 5 min bath in a 5% APTES/acetone solution. The slides were then rinsed with acetone then deionized water and dried with nitrogen gas. For Protein A-treated PDMS microwells, a 10:1 ratio of polymer to crosslinker (Silgard 184 Elastomer) was poured onto 500  $\mu\text{m}$  tall SU-8 columns and cured for at least 2 hrs at 60°C. Slides are then crosslinked to protein using 2 mM bissulfosuccinimidyl suberate (BS3) and then quenched in 2M Tris and 0.3M glycine for 20 min. Next, 20  $\mu\text{L}$  TnT<sup>®</sup> Reticulocyte Lysate is spotted on-chip containing 0.5  $\mu\text{g}$  of protein pairs expressed in pANT7\_nHA and pANT7\_cGST vectors. This solution is incubated for 1.5 hrs in a humid environment at 30°C.

Following incubation, TnT<sup>®</sup> solution-coated slides were moved into a 4°C environment under high humidity for 2 hrs. After incubation, slides were washed in 1 $\times$  PBS with 0.1% Tween-20 (PBST) three times for 5 min per wash. Anti-GST mouse antibody (Cell Signaling Technology, #2624) was applied at 1:500 concentration, followed by 1 hr incubation at room temperature in a humid environment. Slides were then washed in PBST three times for 5 min each. HRP-conjugated anti-mouse (Cell Signaling Technology, #7076) secondary antibody was

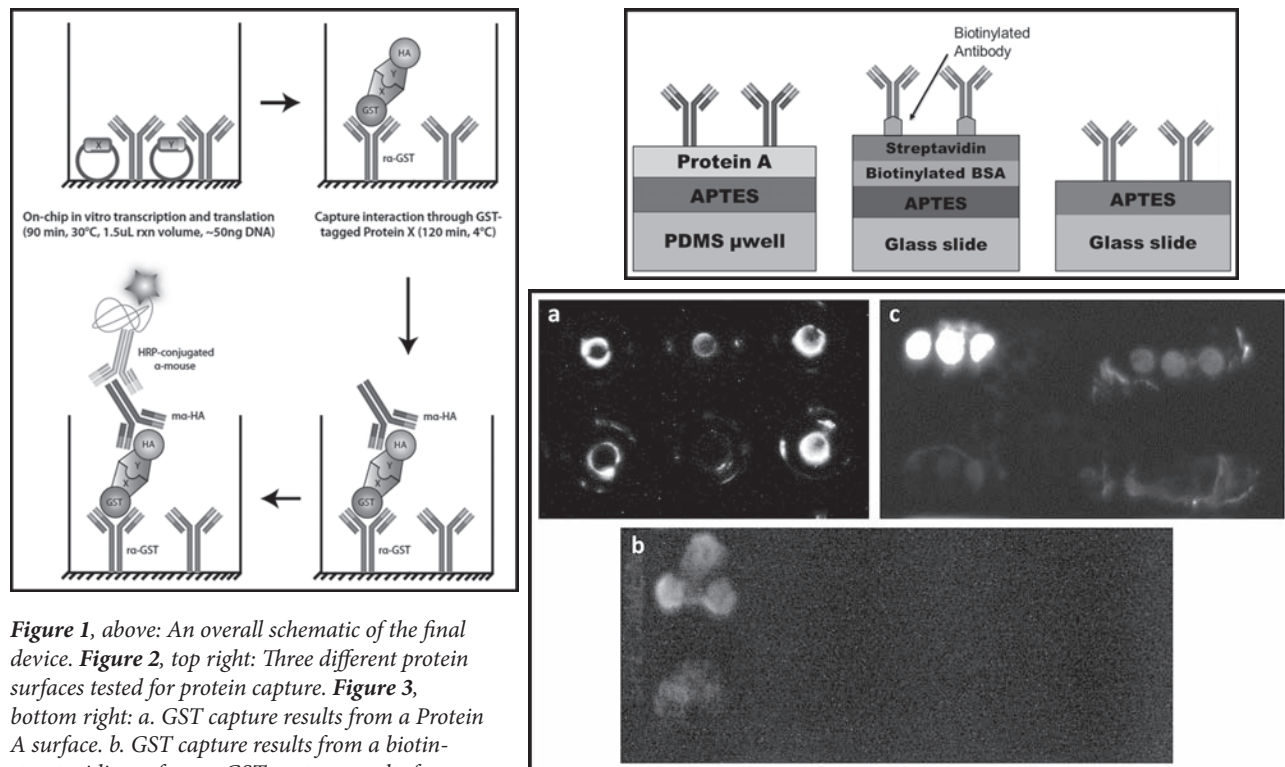


**Figure 1**, above: An overall schematic of the final device. **Figure 2**, top right: Three different protein surfaces tested for protein capture. **Figure 3**, bottom right: a. GST capture results from a Protein A surface. b. GST capture results from a biotin-streptavidin surface. c. GST capture results from an APTES only surface.

then incubated for 1 hr at room temperature in a humid environment. Next, slides were washed with PBS three times for 5 min each. ECL substrate (GE, RPN2232) was then applied and slides were imaged for up to 10 min using a Bio-Rad ChemiDoc system.

### Results and Discussion:

The APTES coated surface with direct application of antibody was the most effective, validated with high specificity when probing for the capture antibody alone. On the Protein A surface, false positives were observed as seen in Figure 3a. In Figure 3a, the rightmost column of luminescing points is composed of a positive control for GST capture on top and a negative control for GST capture on bottom. However, these points are indistinguishable from each other, and probing for GST capture on this protein surface did not yield conclusive results.

The biotin-streptavidin surface had less luminescence than APTES alone when probed solely for capture antibody, as observed in Figure 3b. The leftmost column is a positive control for GST capture; this luminescence was distinguishable from the negative control for GST capture in the rightmost column. The APTES-alone surface was able to repeatedly detect purified protein amounts as low as femtograms of protein as seen in Figure 3c. In Figure 3c, the upper left set of points is the positive control for GST while the negative control is in the middle of the figure. The positive and negative controls are clearly distinguishable

from one another. Also, the lower left portion of Figure 3c illustrates femtogram-levels of GST capture.

### Future Work:

Moving forward, protein tagged for both capture and probe antibodies must be expressed on-chip. Testing a dual-tagged protein will ensure that the antibodies in this procedure are valid to thoroughly measure interaction strength between two proteins. Once the final device is constructed and capable of quantifying tens of thousands of protein-protein interactions at a time, changes in protein-protein networks as a result of environment changes (introduction of drugs, pH, etc.) could be rapidly modeled and evaluated.

### Acknowledgements:

I would like to extend thanks to my mentor Robert Fragoza, Dr. Haiyuan Yu, the Cornell NanoScale Facility Staff, Dr. Lynn Rathbun, and Melanie-Claire Mallison for all of their support. This research was made possible by the support of the National Science Foundation under Grant No. ECCS-0335765, and the National Nanotechnology Infrastructure Network REU Program.

### References:

- [1] Ramachandran, N., et al. *Nat Meth* 5, 535-538 (2008).
- [2] Glick, Y., et al. *Journal of Visualized Experiments*, e3849 (2012).

# Research in a Diagnostic Method for Light Chain Amyloidosis

Shaun Engelmann

Mechanical Engineering, Bradley University

NNIN REU Site: Nano Research Facility, Washington University in St. Louis, St. Louis, MO

NNIN REU Principal Investigator: Dr. Jan Bieschke, Department of Biomedical Engineering, Washington University in St. Louis

NNIN REU Mentor: Kathrin Andrich, Department of Biomedical Engineering, Washington University in St. Louis

Contact: sengelmann@mail.bradley.edu, bieschke@wustl.edu, kandrich@wustl.edu

## Abstract:

Multiple myeloma (MM) is a disease where a plasma B cell clone is excessively replicated in the bone marrow. Systemic light chain amyloidosis (AL) is a complication in some MM patients in which excess light chain (LC) proteins from the plasma B cell clones deposit as amyloid aggregates in various organs, mainly the heart and kidney. The diagnosis of AL and its differentiation from MM is challenging and traditionally is done through invasive tissue biopsies [1]. Early handling of AL is important for effectively treating the condition, so simple and effective diagnostic methods are desired. Our goal was to develop a technique for AL diagnosis based on LC proteins from MM patients excreted in urine using an *in vitro* aggregation assay. First, *in vitro* amyloid fibril formation was optimized in order to create fibrils. Buffer pH, NaCl concentration, and temperature were varied in aggregation assays, and the aggregation kinetics were monitored using the amyloid-specific dye Thioflavin T (ThT) [2]. Samples were also shaken during aggregation, and the time intervals between shaking were also varied. This was done to alter the formation of amyloid seeds, which act as bases for LC proteins add to [3]. Amyloid aggregate morphologies then needed to be confirmed, which was done through atomic force microscopy (AFM) and transmission electron microscopy (TEM). This was performed and conditions that generated LC aggregates with fibrillar structures within a week were found.

## Methods:

**Aggregation Assays.** Aggregation assays were performed in a 96-well plate and monitored by ThT fluorescence with a Tecan Infinite F200 multimode reader. The aggregation buffers consisted of either 50 mM Glycine (pH 2.8) or sodium phosphate buffer (NaP, pH 7.2). The buffers contained either 0, 50, 150, or 300 mM NaCl. They also contained 10 mM dithiothreitol, 20  $\mu$ M ThT, and 20  $\mu$ M LC protein extracted from AL patient urine. LC proteins were aggregated in three separate sessions – one in 25°C that was shaken every 15 minutes, another in 37°C that was shaken every 15 minutes, and the last one in 37°C that was shaken every 30 minutes. Fluorescence was read at an excitation of 436 nm and an emission of 485 nm.

**Imaging.** AFM images were gathered from protein adsorbed to mica using tapping mode on a Bruker Dimension Atomic Force Microscope (AFM) and Etalon HA\_NC/15 tips. The solutions adsorbed to mica were diluted 1:4 with either glycine or NaP. Images with

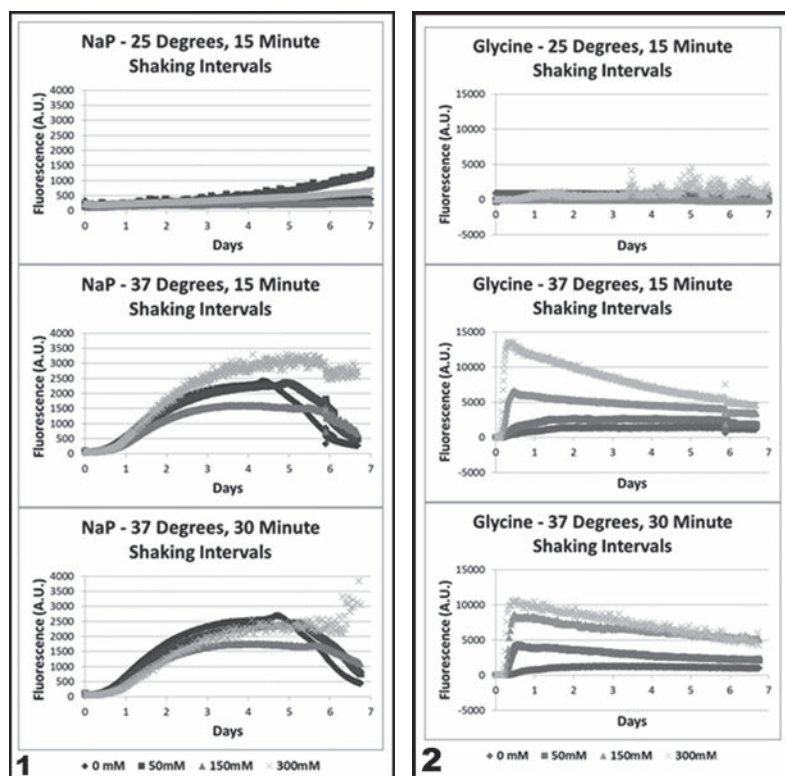
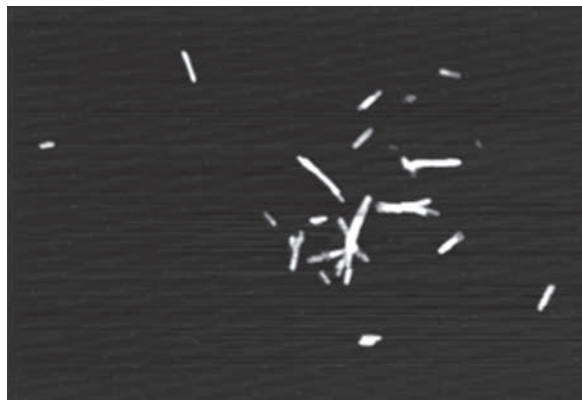
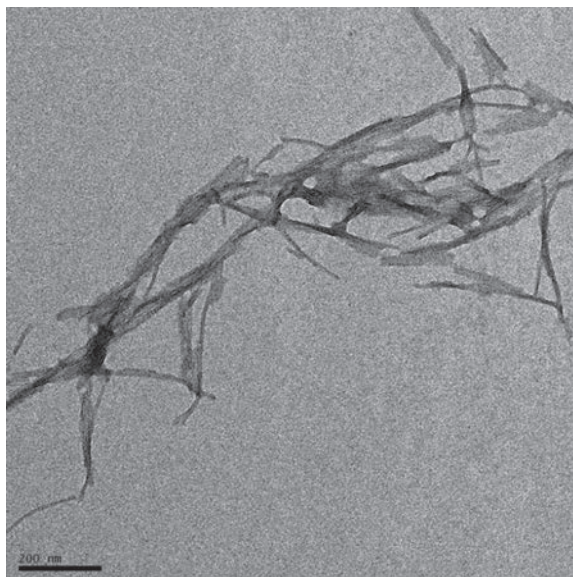


Figure 1: Plots showing LC seven day aggregations in NaP with different conditions.  
Figure 2: Plots showing LC seven day aggregations in glycine with different conditions.



**Figure 3, above:** AFM image confirming amyloid formation. The image is of an area 3.3  $\mu\text{m}$  wide. **Figure 4, right:** TEM image of LC amyloids. Scale bar is 200  $\mu\text{m}$  wide.



transmission electron microscopy (TEM) were taken from protein solution adsorbed to Ted Pella 200 mesh carbon coated copper grids. Negative staining was originally performed with uranyl acetate replacement (UAR) stain. A switch to 4% uranyl acetate (UA) was made later on.

## Results and Discussion:

**Aggregation Assays.** The plots shown in Figures 1 and 2 represent the aggregation assays performed with the LC proteins. It can be seen that ThT fluorescence did increase in the aggregations performed at 37°C, which indicates the formation of amyloid structures. The aggregations performed in NaP at 37 degrees slowly reached a maximum over the aggregations. The aggregation occurred much faster in glycine, followed by a slow decrease in fluorescence after peaking. The aggregation performed in NaP in 25°C did not peak, but did increase by the end of seven days. This slowed fluorescence increase when compared to the 37°C aggregations suggests that temperature alterations could be used to control aggregation. The difference in aggregation kinetics between shaking every 15 minutes when compared to 30 minutes was negligible. NaCl concentration had a positive correlation with fluorescence amplitudes and accelerated aggregation kinetics in glycine, but such a correlation was not seen in NaP.

**Imaging.** AFM and TEM were used to determine if aggregates with fibrillar morphologies were formed during the aggregations. Previously, LC amyloid formation was only observed after 24 day aggregation with our proteins. An image of our LC amyloid fibrils is shown in Figure 3. It is from the seven day aggregation sample performed in glycine that contained no NaCl, and was shaken for 5 s every 15 minutes at 37°C. TEM imaging of the proteins proved to be difficult at first, as UAR stain resulted in precipitate that appeared like fibrillar protein structures even on grids with no protein adsorbed. This discovery

encouraged the switch to 4% UA that was used to identify fibrillar structures. A TEM image of our amyloid fibrils is shown in Figure 4.

## Conclusions:

AL is currently difficult to diagnose without invasive medical procedures. Multiple conditions for *in vitro* aggregation of LC isolated from AL patient urine were investigated to determine if it could be used in AL diagnosis. Temperature and NaCl concentration were shown to affect aggregation, suggesting that control over LC amyloid aggregation is possible. AFM and TEM were used to show amyloids were formed during aggregation assays. The optimized aggregation protocol accelerated LC amyloid fibril formation to a few days instead of three weeks, encouraging its future utility as a diagnostic tool.

## Acknowledgements:

I would like to thank Dr. Jan Bieschke, Kathrin Andrich, Nathan Reed, and Remya Nair of Washington University in St. Louis for all their help and the opportunity to work on this project. I would also like to thank Melanie-Claire Mallison of Cornell University, and the NNIN and the NSF for the invitation to participate in the NNIN REU program, and for funding under Grant No. ECCS-0335765.

## References:

- [1] Merlino, G; "Molecular Mechanisms of Amyloidosis"; *The New England Journal of Medicine*, 349, 583-596 (2003).
- [2] Levine, H; "Quantification of Beta-Sheet Amyloid Fibril Structures with Thioflavin T"; *Methods in Enzymology*, 309, 274-284 (1999).
- [3] Dobson, C; "Protein Folding and Misfolding"; *Nature*, 426, 884-890 (2003).

## Optimization of Nanoparticle Delivery to Plants: Do Nanoparticle Properties Affect Cellular Internalization?

**Christina Franke**

**Biomedical Engineering, Case Western Reserve University**

**NNIN REU Site: Nano Research Facility, Washington University in St. Louis, St. Louis, MO**

NNIN REU Principal Investigator: Dr. Pratim Biswas, Energy, Environmental and Chemical Engineering, Washington University in St. Louis

NNIN REU Mentor: Dr. Ramesh Raliya, Department of Energy, Environmental and Chemical Engineering, Washington University in St. Louis

Contact: christina.franke@case.edu, pbiswas@wustl.edu, rameshraliya@wustl.edu

### Abstract:

To minimize damage to the ecosystem and enhance sustainability in farming practices, intervention of nanotechnology in agriculture has increased in recent years. The purpose of this work was to study the effects of various gold nanostructures of 30 to 80 nm delivered by foliar application on uptake, translocation, and accumulation in a watermelon plant. Cellular uptake and translocation of gold nanoparticles from leaf to root was confirmed by ICP-MS. Accumulation and transport of nanoparticles depends on nanoparticle shape and application method.

### Introduction:

Gold nanoparticles (AuNPs) have been extensively studied in recent years due to the abundance of their potential applications to biological systems; being biologically inert, AuNPs are less toxic to cells than nanoparticles of other materials [1]. Because they also adsorb DNA easily, AuNPs can be used in agricultural biotechnology for delivery of genetic material to plant cells [2] and detection of plant viruses [3]. Researchers have asked the questions: How do we measure the ecotoxicity of these emerging technologies, and how do we make these technologies safe and sustainable? To answer these questions, it is essential to understand the fundamental mechanisms of morphology-dependent cellular uptake of gold nanoparticles and their subsequent fate in a plant system.

### Experimental Procedure:

**Gold Nanoparticle Synthesis and Characterization.** AuNPs of spherical, cubic, rhombic dodecahedral (RD), and rod morphologies were chemically synthesized using seed-mediated methods [4,5] and characterized for physical diameter, hydrodynamic size and zeta potential using transmission electron microscopy (TEM) and dynamic light scattering respectively, and surface plasmon resonance determined with UV-visible spectrophotometry. Finally, concentrations of nanoparticles in suspension were analyzed using inductively coupled plasma-mass spectroscopy (ICP-MS).

**Application of Nanoparticles to Plant.** Foliar aerosol delivery of nanoparticles (NPs) may help to reduce environmental harm by increasing uptake by plants

and limiting contamination of the soil environment [6]. Consequently, we employed a foliar application of AuNPs that delivered them through the stomatal openings, avoiding direct contact with the soil ecosystem. The phloem subsequently transports NPs from shoot to root [7]. Watermelon plants (*Citrullus lanatus*) were chosen for this experiment due to their large stomata and vessel size, which may facilitate NP translocation [6]. In this study, drop-cast and aerosol based foliar applications were compared to determine the effect of applied droplet size on AuNPs-plant interactions. The drop-cast method uses an auto pipette to render  $800 \pm 175 \mu\text{m}$  droplets that may contain soft agglomerations of nanoparticles. An aerosol method, the atomizer, breaks up agglomerations, producing tiny droplets in the mean size range of  $250 \pm 50 \text{ nm}$ . Real-time applied particle size was monitored using scanning mobility particle size (SMPS) measurement.

**Nanoparticle Uptake Analysis.** Plants were harvested 48 hours after applying the nanoparticles and washed to remove soil. Roots, stems, and leaves of each plant were separated, dried, and digested. The resulting concentration of elemental gold in each plant section was analyzed with the aid of ICP-MS.

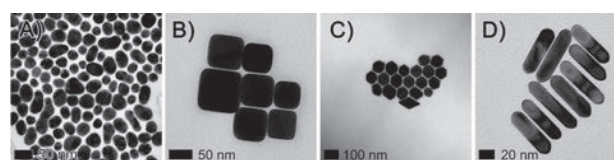


Figure 1: TEM images of gold (A) spheres, (B) truncated cubes, (C) rhombic dodecahedra, and (D) rods.

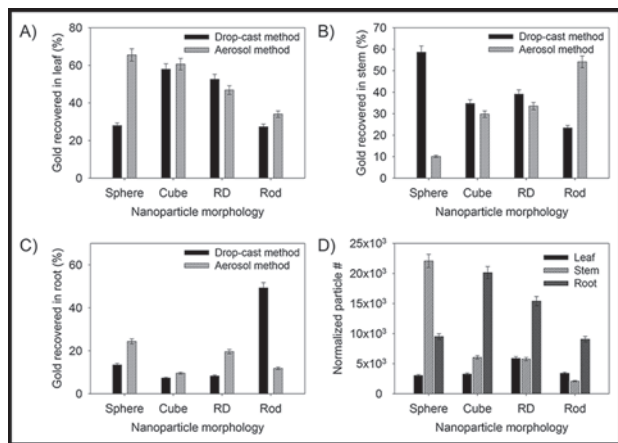


Figure 2: Percent of total gold in plant that was recovered by ICP-MS in (A) root, (B) shoot, and (C) root sections of treated plants, comparing results of drop-cast and aerosol methods. (D) Number of particles recovered in sections of aerosol-treated plants, normalized to number concentration of particles.

	Particle Size* (nm)	Hydrodynamic Size <sup>c</sup> (nm)	PDI <sup>d,e</sup>	$\lambda_{max}$ * (nm)	Zeta Potential <sup>f</sup> (mV)	Concentration, Au (ppm)
Sphere	35	61.0±31.6	0.457	527	-40.5	$2.29 \times 10^3$
Cube	70	99.2±25.1	0.034	563	56.7	$1.12 \times 10^4$
Rhombic	65	99.8±30.4	0.066	550	64.3	$1.18 \times 10^4$
Dodecahedra	20, 60 <sup>g</sup>	114.1±52.1	0.296	816	43.9	$1.44 \times 10^3$

\* Mean geometric diameter, obtained from TEM images (Fig. 1)  
<sup>b</sup> Diameter, length  
<sup>c</sup> From DLS, intensity particle size distribution  
<sup>d</sup> Polydispersity index  
<sup>e</sup> Surface Plasmon Resonance, obtained from maximum UV-vis peak

Table 1: Characterization data for nanoparticles in aqueous suspension.

	Method	Amount in leaf (%)	Amount in stem (%)	Amount in root (%)	Percent difference, drop-cast vs aerosol
Sphere	Drop-cast	28.0	58.6	13.4	10.9
	Aerosol	65.5	10.1	24.4	
Cube	Drop-cast	57.9	34.8	7.3	2.3
	Aerosol	60.6	29.8	9.6	
Rhombic	Drop-cast	52.6	39.1	8.3	11.3
	Aerosol	46.8	33.6	19.6	
Rod	Drop-cast	27.4	23.4	49.3	37.4
	Aerosol	34.0	54.1	11.8	

Table 2: Results of elemental analysis of gold in plant sections by ICP-MS.

## Results and Conclusions:

All characterization data is depicted in Table 1. Images confirming nanoparticle geometric diameters and morphologies were obtained with TEM (Figure 1). Uptake and distribution of AuNPs throughout the plant system was confirmed by ICP-MS. The measured concentrations of elemental gold in each sample were normalized by the dried mass of the plant section, and this data was processed to determine the percent of recovered gold in each plant section (Figure 2).

Comparing the two application methods, the aerosol method enhanced the transport of low aspect ratio NPs (Sphere, Cube, RD) while the larger droplet size applied by the drop-cast method improved the transport of high aspect ratio, rod-shaped NPs. For sphere, cube, and RD morphologies respectively, the increase in translocation rate of the aerosolized versus drop-cast nanoparticles was 10.9, 2.3, and 11.3%, whereas a 37.4% decrease in translocation rate was observed for the nanorods (Table 2).

Among drop-cast NPs, a trend in the efficacy of translocation (percent of recovered gold accumulated in roots) was observed as: rod (49.3%) > sphere (13.4%) > RD (8.3%) > cube (7.3%) (Table 2). In order to account for any discrepancies in the number of particles applied by the aerosol method, the aerosol results were normalized by the acquired concentration of gold obtained by our SMPS number concentration measurements.

From these normalized results (Figure 2D), a trend in the efficacy of translocation (number of particles recovered in root) was observed as: cube ( $2.0 \times 10^4$ ) > RD ( $1.5 \times 10^4$ ) > sphere ( $9.5 \times 10^3$ ) > rod ( $9.0 \times 10^3$ ), a trend that again suggests the aerosol application method results in improved translocation of low aspect ratio particles. Further experiments are needed to confirm these results, as well as to study the effects of other nanoparticle properties on their uptake and fate.

## Importance of the Study:

From the morphology-dependent trends in nanoparticle translocation, it can be concluded that accumulation and transport of nanoparticles depends on nanoparticle shape. Our evidence also suggests that different application methods may be optimal for delivery of different morphologies of nanoparticles to plants.

## Acknowledgements:

I would like to thank Dr. Pratim Biswas, my mentor Dr. Ramesh Raliya, and the NRF staff for their guidance and expertise. This project was made possible by the NNIN REU Program under NSF Grant No. ECCS-0335765.

## References:

- [1] Shukla, R., et al. Langmuir, 2005. 21(23): p. 10644-10654.
- [2] Nair, R., et al. Plant Science, 2010. 179(3): p. 154-163.
- [3] Zhao, W., et al. Biosensors and Bioelectronics, 2011. 26(10): p. 4241-4244.
- [4] Becker, R., et al. J Colloid Interface Sci, 2010. 343(1): p. 25-30.
- [5] Wu, H.-L., et al. Langmuir, 2010. 26(14): p. 12307-12313.
- [6] Wang, W.-N., et al. J Nanopart Res, 2013. 15(1): p. 1417-1430
- [7] Wang, Z., et al. Environ Sci Technol, 2012. 46(8): p. 4434-4441.

## Development of a Microfluidic Mimic of the Human Microvasculature to Study Sickle Cell Disease

Michelle Galarneau

Chemical and Biomolecular Engineering, University of Notre Dame

**NNIN REU Site: Minnesota Nano Center, University of Minnesota-Twin Cities, Minneapolis, MN**

NNIN REU Principal Investigator: Dr. David Wood, Department of Biomedical Engineering, University of Minnesota-Twin Cities

NNIN REU Mentor: Xinran (Daniel) Lu, Department of Biomedical Engineering, University of Minnesota-Twin Cities

Contact: mgalarne@nd.edu, dkwood@umn.edu, luxx794@umn.edu

### Introduction:

Often characterized by severe pain crises and organ damage due to hypoxia, sickle cell disease (SCD) is a genetic disorder caused by a mutation in the hemoglobin molecule of red blood cells (RBCs) [1]. This mutation leads RBCs to stiffen under hypoxic conditions, in turn making the cells more susceptible to obstructing blood flow. Known as a vaso-occlusive crisis (VOC), this obstruction stands as the major cause of morbidity and mortality in SCD [2]. Currently, hydroxyurea (HU) is the sole FDA-approved drug treatment option available to patients, and yet HU is ineffective in one-third of those treated [3]. Consequently, there is a clear need for more effective drug treatments, as well as a screening platform to evaluate drug efficacy. Thus, we created an *in vitro* microfluidic disease model to screen new drug treatments. A remarkable alternative to *in vivo* techniques, microfluidics provides a convenient and reproducible platform with which to simulate the rheological occurrences of SCD.

### Methods:

The optimal design for the device was to produce a linear oxygen tension gradient across the microvasculature, mimicking physiological conditions. AutoCAD was used to design the device layers.

Design considerations for the microvasculature layer included channel width (vessel diameter), bifurcations, segmental length, total length, and channel height. The most important consideration was channel width, as the range of diameters across vessels composing the microvasculature (small arteries, arterioles, capillaries, venules, small veins) differs according to the anatomical region of interest. To account for these differences, we designed twelve microvasculature layers featuring varied channel width ranges. The design we fabricated for experimental purposes has a range of 10  $\mu\text{m}$  to 60  $\mu\text{m}$ , which is both physiologically accurate and amenable to the dimensional constraints imposed by polydimethylsiloxane (PDMS). In addition, the design we fabricated and tested was 3 mm in total length.

We then designed a layer containing a series of gas channels that, when overlaid onto the microvasculature layer, produced an oxygen tension gradient. The oxygen layer we fabricated consisted of five gas channels, whose dimensions were determined via finite element modeling of oxygen diffusion in COMSOL.

We used soft photolithography with SU-8 2000 series photoresist to fabricate the master for each layer. We then cast these masters with PDMS, and the layers were subsequently cured and bonded to each other and to a glass slide via oxygen plasma treatment.

Specific oxygen tensions were created by cycling an air stream and a  $\text{N}_2$  stream via solenoid valves. The duty cycles necessary to produce the desired tensions were specified in a MATLAB/Arduino system. To ensure proper calibration, oxygen tensions were also measured at each gas outlet.

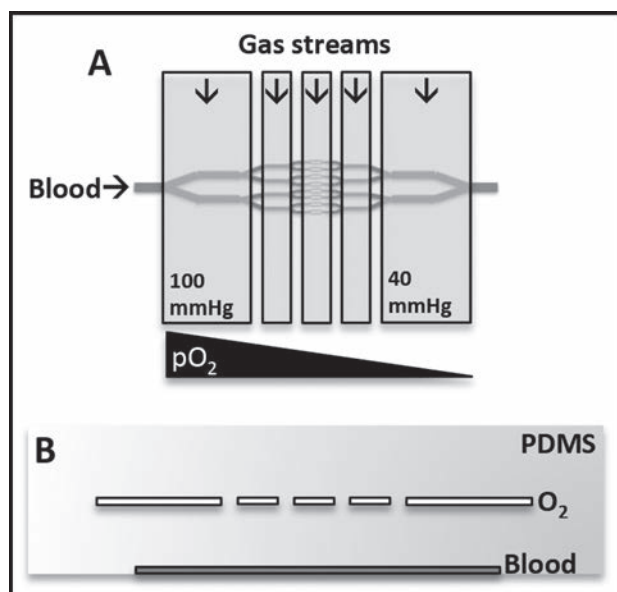


Figure 1: A. Top-down view of device. B. Cross-sectional view of device.

## Results and Discussion:

During the modeling phase of this project, we found the most important parameters in obtaining the optimal design to be width of the gas channels, distance between the gas channels, and gap width between the microvasculature and oxygen layers. Furthermore, while a large gap width between layers corresponded to a more linear oxygen gradient, we sought to minimize this gap width for construction purposes. Thus, series of stationary studies were run in COMSOL, each for a specific gap width, and tension data across the microvasculature layer were plotted. After fitting a line to the data and determining variance for each data point, a threshold for the average variance was set (this threshold was applied to all five-channel oxygen layer designs) and an optimal gap width was obtained. Figure 2 displays the modeled tension curve for this final design.

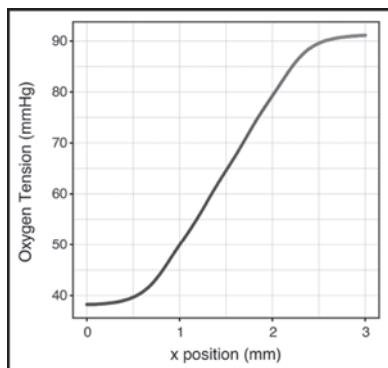


Figure 2: Finite element model of oxygen gradient.

To validate the oxygen gradient experimentally, we used 4 mM tris(2,2'-bipyridyl)dichlororuthenium(II) hexahydrate (RuBPY), an  $O_2$ -sensitive dye whose luminescence is quenched in the presence of  $O_2$ . We perfused this solution through channels directly beneath the oxygen layer (i.e., channels analogous to the microvasculature layer), and measured luminescence intensity values using an inverted epifluorescence microscope. Intensity readings were then converted into tensions based on a calibration curve. These tensions are plotted in Figure 3.

Characterization with RuBPY showed that the experimental oxygen tension gradient has a decreasing trend; however, it is not perfectly linear, as the model predicts. Using a luminophore with a higher sensitivity, as well as minimizing the presence of unwanted features/

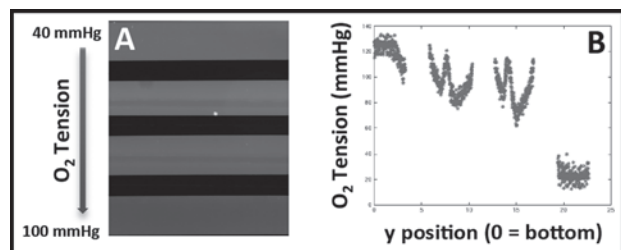


Figure 3: A. Image of RuBPY luminescence intensity gradient across four channels. Light regions correspond to low  $O_2$  tensions. B. Experimental  $pO_2$  vs. position data.

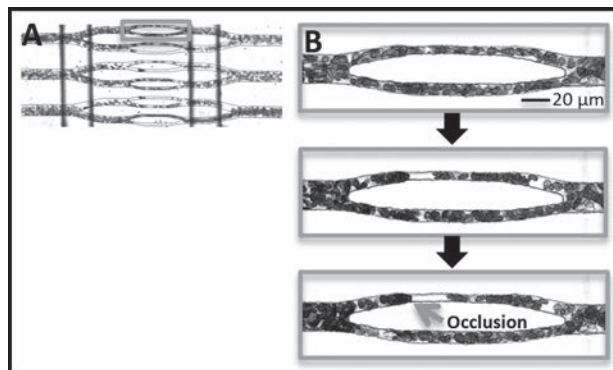


Figure 4: A. Brightfield image of a region of the device, through which sickle cell blood flows. B. Time progression of blood flowing through the  $10\ \mu\text{m}$ -wide channels of device as the oxygen gradient develops. In the bottom image, gradient is fully developed.

debris in the device, would likely lead to validation of a more linear gradient.

We experimented with running a sickle cell blood sample through the device under a pressure of 1 psi. Upon gradient development, we observed significant slowdowns in blood flow, as well as occlusions within the capillary-sized channels (Figure 4). Knowing that sickle RBCs respond to these conditions, such experiments lend insight into the mechanical effects on the rheology of SCD.

## Conclusions:

We developed a microfluidic device to serve as a SCD model, and determined that the device is capable of reproducing hallmark rheological occurrences of the disease. By capturing even more physiologically relevant parameters in future designs, we hope this device ultimately becomes an accurate, accessible means of screening new drug treatments for SCD.

## Acknowledgements:

I would like to thank Dr. David Wood, Daniel Lu, and all other members of the Living Devices Lab and the Minnesota Nano Center for their incredible guidance. I would also like to acknowledge the NNIN REU Program and the NSF for funding this research under Grant No. ECCS-0335765.

## References:

- [1] Belcher, J.D., et al. "Activated monocytes in sickle cell disease: potential role in the activation of vascular endothelium and vaso-occlusion." *Blood* 96.7 (2000): 2451-2459.
- [2] Wood, D.K., et al. "A biophysical indicator of vaso-occlusive risk in sickle cell disease." *Science trans. medicine*, 4.123 (2012): 1-7.
- [3] Fathallah, H., and G.F. Atweh. "Induction of fetal hemoglobin in the treatment of sickle cell disease." *American Society of Hematology Education Program Book 2006.1* (2006): 58-62.

# Small Interfering RNA Delivery for the Treatment of Hereditary Bone Disease

Staci Hill

Chemistry, Middlebury College

**NNIN iREU Site: National Institute for Materials Science (NIMS), Tsukuba, Ibaraki, Japan**

NNIN iREU Principal Investigator: Dr. Nobutaka Hanagata, Nanotechnology Innovation Station, NIMS, Tsukuba, Japan

NNIN iREU Mentor: Xianglan Li, Nanotechnology Innovation Station, National Institute for Material Science, Tsukuba, Japan

Contact: staciannahill@gmail.com, hanagata.nobutaka@nims.go.jp, li.xianglan@nims.go.jp

## Introduction:

Osteogenesis imperfecta (OI) is a heterogeneous bone disease classified into eight different types based on phenotype and genotype [1]. OI type V is caused by a mutation of interferon-induced transmembrane protein 5 (IFITM5) [2]. The mutant protein has an additional five amino acids (Met-Ala-Leu-Glu-Pro) at the N-terminus in individuals with OI type V [2].

IFITM5 is an osteoblast-specific membrane protein previously seen to be a positive regulator for bone formation in *in vitro* studies [3]. Despite this evidence, recent studies show that bone formation of *Ifitm5* knockout mice are comparable to bone formation of the wild type [3,4]. The discrepancy between the *in vitro* and *in vivo* experiments suggests that there exists an *in vivo* mechanism in place to ensure healthy bone formation in the absence of the protein. Given that OI type V is caused by a mutation in IFITM5, suppressing IFITM5 protein translation should restore healthy bone growth for individuals with the disease.

In this report, small interfering RNA (siRNA) was used to suppress the translation of the mutant protein IFITM5 *in vitro*. Four transfection reagents were tested using mouse osteoblast cells: DOTAP, Lipofectamine2000, Lipofectamine RNAiMAX (RNAiMAX), and calcium phosphate (CaP) nanoparticles. Following transfection, cells were lysed to extract and purify RNA. RNA was subsequently converted to DNA using PCR, and q-PCR was used to determine relative gene expression. Among the transfection reagents used, RNAiMAX was the most effective, suppressing gene translation by an average of 60%.

## Materials:

Mouse osteoblasts (MC3T3) and MEM-alpha medium (10% FBS) were used throughout the study. Lipofectamine2000 and RNAiMAX were purchased from Invitrogen Corporation by Life Technologies (Carlsbad, CA, USA). DOTAP was purchased from Roche Diagnostics GmbH (Mannheim, Germany). CaP nanoparticles were made using reagents from the CalPhos Mammalian Transfection Kit obtained from Clontech Laboratories, Inc.

(Mountain View, CA, USA). Isogen used for RNA extraction was obtained from Nippon Gene Co. (Tokyo, Japan). Real-time PCR (q-PCR) was carried out on a LightCycler System. Glycerol 3-phosphate dehydrogenase (GAPDH) was used as a housekeeping gene.

## Methods:

All incubations not specified were carried out at 37°C in a 5% CO<sub>2</sub> controlled environment. All siRNA complexes were made following manufacturer protocol.

For liposomal transfection, cells were seeded at 1.5 × 10<sup>4</sup> cells/cm<sup>2</sup> on six well plates. Cells were immediately exposed to the transfection reagent complexed with either IFITM5 siRNA (50 pmol/well) or control siRNA (SCN01) (50 pmol/well).

	Condition A	Condition B	Condition C
Total siRNA (ug)	0.34	0.68	1.60
[siRNA] (ug/mL)	20	20	40
[CaP] : [siRNA]	5 : 1	2.7 : 1	2.7 : 1

For CaP nanoparticle transfection, cells were seeded overnight at 7.0 × 10<sup>3</sup> cells/cm<sup>2</sup>. The next day, medium was replaced with a mix of serum free medium and CaP nanoparticles complexed with either IFITM5 siRNA or SCN01 siRNA. Table 1 details the three conditions. Three hours after transfection, serum-free medium incubated in a 10% CO<sub>2</sub> environment was added so that the medium volume was doubled. The addition of slightly acidic medium aided the dissolution of the nanoparticles.

After a 24 hr incubation period, all wells were replaced with fresh medium and a mix of mutant IFITM5 plasmid (2 ug/well) and Lipofectamine2000 transfection reagent. A subsequent incubation period of 24 hours ensured complete transfection and replication of the genetic material.

Cells were washed with PBS, and then total RNA was extracted with Isogen according to manufacturer protocol.

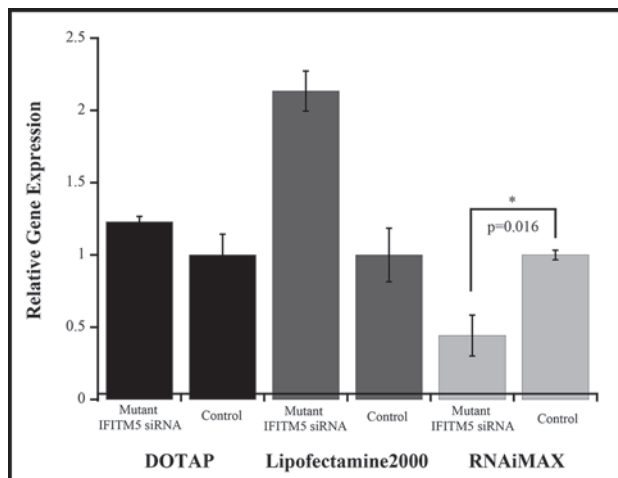


Figure 1: Relative expression of mutant IFITM5 genetic material. Three different commercially available liposomal transfection reagents are compared.

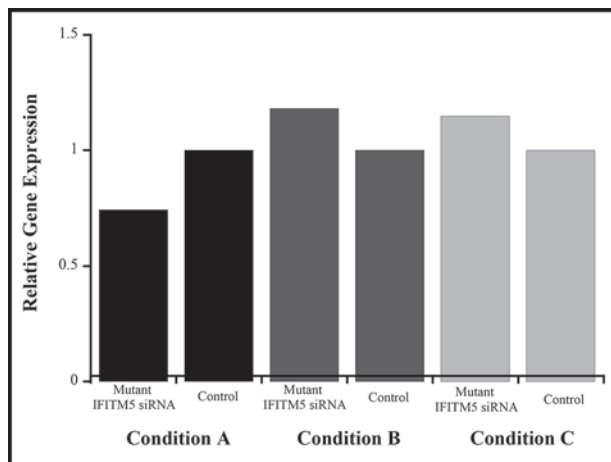


Figure 2: Relative expression of mutant IFITM5 genetic material. Three different compositions of CaP nanoparticles are compared.

Concentration of extracted RNA was determined using UV/Vis spectroscopy. RNA was diluted to 500 ng/uL and then converted to DNA using reverse transcriptase. Resulting DNA was diluted to 5 ng/uL. Expression was quantitatively measured using the cross-point of amplification as determined by real-time polymerase chain reaction (q-PCR).

## Results and Discussion:

Figure 1 and 2 show the relative expression of mutant IFITM5 genetic material, comparing osteoblasts transfected with IFITM5 siRNA and control siRNA. Figure 1 highlights the liposomal transfection reagents studied, among which RNAiMAX suppressed IFITM5 gene expression 60% relative to the control. DOTAP and Lipofectamine2000 both failed to suppress gene expression. The success of RNAiMAX is difficult to ascertain because its chemical and structural properties are not distributed by the manufacturer. Additionally, the release mechanism of siRNA into the cell after endocytosis is still unclear. These conceptual barriers prevent a detailed explanation for siRNA suppression using RNAiMAX. Factors that may influence the transfection efficiency include the size of the liposome complex and its chemical composition.

Figure 2 shows the results from individual studies using CaP nanoparticles as the siRNA transfection reagent. The condition with a greater CaP:siRNA ratio and lower concentration of siRNA was seen to suppress gene expression 30% relative to the control.

Because siRNA is foreign genetic material, excess siRNA can induce apoptosis while too little siRNA would decrease the knockdown effect. Therefore, concentration of siRNA is critical to the survival of the cells and transfection

efficiency. This experiment suggests that 20 ug/mL of siRNA is sufficient to suppress gene expression, but the CaP study included a single experiment per variation. The reproducibility of these results is yet to be determined.

## Conclusions:

The transfection reagent RNAiMAX demonstrates that gene suppression is feasible on the cellular level. Due to the limited information of the compound, RNAiMAX is not a desirable method for *in vivo* studies at this time. CaP nanoparticles as a known biologically degradable compound should be investigated further to determine if it is a viable method to suppress gene expression both on the cellular and physiological level. Furthermore, the method of siRNA delivery subsequent to endocytosis should be investigated for optimization of transfection efficiency.

## Acknowledgements:

The NSF (Grant No. ECCS-0335765) and National Nanotechnology Infrastructure Network International Research Experience for Undergraduates (NNIN iREU) Program are acknowledged for funding and supporting this research. In addition, the unwavering support of Dr. Hanagata-san and inspiring mentorship under Li-san is greatly appreciated.

## References:

- [1] Semler, O., et al. *Am. J. Hum. Genet.* 2012, 91 (2), 349-357.
- [2] Cho, T.-J., et al. *Am. J. Hum. Genet.* 2012, 91 (2), 343-348.
- [3] Hanagata, N., et al. *J. Bone Miner. Metab.* 2011, 29 (3), 279-290.
- [4] Hanagata, N. *J. Bone Miner. Metab.* 2015, 1-9.

# Optimization and Characterization of Au Nanoparticle-DNA Conjugate Devices

**Joseph P. Hittinger**

**Chemical and Biomolecular Engineering, Vanderbilt University**

**NNIN REU Site: Washington Nanofabrication Facility and Molecular Analysis Facility, University of Washington, Seattle, WA**

*NNIN REU Principal Investigators: Dr. James M. Carothers, Chemical Engineering, University of Washington;*

*Dr. David G. Castner, Chemical Engineering and Bioengineering, University of Washington*

*NNIN REU Mentor: Michael A. Newton, Chemical Engineering, University of Washington*

*Contact: joseph.p.hittinger@vanderbilt.edu, jcaroth@uw.edu, castner@uw.edu, manewton@uw.edu*

## Abstract:

In this project, spherical gold nanoparticles (AuNP) were loaded with deoxyribonucleic acid (DNA) oligonucleotides to make a series of single- and double-stranded conjugates, which were characterized via various established methods to optimize loading efficiency and functionality. Characterization methods used include ultraviolet-visible spectrophotometry (UV-Vis) to measure absorbance and estimate loading efficiency; dynamic light scattering (DLS) and zeta potential (ZP) measurements to estimate conjugate size and extent of aggregation; and gel electrophoresis to separate and analyze conjugates based on size and charge. Toehold-mediated strand displacement DNA fluorescent gates were tested in order to relate characterization to device performance. Salt aging to 100 mM NaCl provided high loading ( $131 \pm 7$  strands per particle) with low particle aggregation and relatively high hybridization efficiency ( $58 \pm 6\%$ ), while maintaining strand displacement logic gate device capability.

## Introduction:

AuNPs have been broadly studied as platforms for small molecule, antibody, and aptamer delivery to cells because of the variety of functional groups that can be bound to the AuNP surface [1]. However, many reports of AuNP applications in biomedical diagnostics and therapeutics lack sufficient characterization to fully understand and optimize their loading [2,3].

This project aimed to utilize the multitude of characterization techniques at our disposal in order to provide a more holistic understanding of AuNP loading. Optimizing our AuNP-DNA conjugates while balancing device performance can provide greater functionality for applications such as high payload drug delivery agents.

## Experimental Procedure:

We began with approximately 14 nm diameter, citrate-capped AuNPs synthesized via the citrate reduction method [4]. We made a series of conjugates at varying NaCl concentrations (50, 100, 200 mM) to establish a trend between DNA loading and salt concentration. The single-strand DNA covered AuNPs (ssAuNPs) were synthesized by adding the initial DNA oligo capture strand to the AuNP solution in a molar ratio of 195 DNA/AuNP, then left to shake for approximately 16 hours [5]. The conjugates were then salt-aged to the desired NaCl concentrations over a period of six hours to minimize aggregation, then centrifuged for 30 minutes at 10,500 RCF.

Supernatant was collected in separate tubes and the conjugates were resuspended in the same volume and concentration NaCl. This was done three times total. Residual DNA in the supernatant was quantified via ultraviolet visible spectrophotometry (UV-Vis) absorbance measurements to estimate DNA loading on the AuNP surface.

The double-stranded DNA covered AuNPs (dsAuNPs) were synthesized by adding the complementary oligonucleotide to the ssAuNP solution in a 1:1 molar ratio based on the single-stranded loading estimate. They were then left to shake for approximately two hours before quantifying DNA hybridization with UV-Vis as before. Dynamic light scattering (DLS) and zeta potential (ZP) measurements of the conjugates were taken before conducting a second trial at the same concentration (100 mM) to test repeatability. Gel electrophoresis (1.5% agarose gel) was also performed on all samples from each trial.

Single- and double-stranded conjugates were synthesized with a new set of oligos capable of efficient strand displacement [6]. For this trial, the hybridizing strand had a ROX fluorophore modification that upon hybridization would be close to the AuNP surface. Toe-hold mediated strand displacement reactions were performed on this batch of conjugates in order to test device performance. A fluorometer (2x Gain) was used to monitor fluorescence during hybridization and strand displacement (two hours each).

## Results:

By varying the salt concentration of the conjugate solution, we found hybridization efficiency increased with increasing NaCl concentration (Figure 1). DLS measurements gave us an indication of the relative extent of aggregation for each salt concentration. While conjugates synthesized in 200 mM NaCl showed the highest hybridization efficiency, they also showed the most aggregation (Figure 2).

ZP measurements of the conjugates were distinctly different than that of the bare AuNP control, varying by an average of about 20 mV. The conjugates had ZP values around -40 mV, indicating particle stability.

We used 100 mM NaCl for our second trial testing repeatability. The conjugates synthesized at this concentration showed slightly reduced hybridization efficiency than the higher salt concentration, but also showed less aggregation (about 3% by volume).

Slight mobility differences between the ssAuNPs and dsAuNPs in gel electrophoresis (Figure 3) indicated hybridization had occurred in both trials. The gel for the 100 mM NaCl conjugates also showed our process to be repeatable.

Our final round of conjugates employing new oligos tested device performance via strand displacement (Figure 4). The hybridizing strand had a fluorescent dye modification (ROX) that quenched in proximity to the AuNP, as seen in the fluorescence decrease during hybridization in Figure 4. As the invading strand displaced the fluorescent oligo, fluorescence increased again as expected. This successful strand displacement proved the capability of our device and assay.

## Conclusions:

Our results show promising possibilities for attaining optimal DNA loading efficiency on spherical gold nanoparticles. Our data suggests salt-aging to 100 mM NaCl could be a good starting point from which to continue studying characterization and performance of nucleic acid devices and their relation to DNA loading. In the future we would like to pursue different DNA tethers, vary the length of the carbon linker chain, and incorporate aptamers onto the device to study the full extent of its performance. Further quantification of device performance is possible based on the tested strand displacement assay.

## Acknowledgments:

This project was made possible by the National Science Foundation [ECCS-0335765], National Nanotechnology Infrastructure Network Research Experience for Undergraduates (NNIN REU) Program, University of Washington, Molecular Engineering & Sciences Institute, and NESAC/BIO [NIH NIBIB EB-002027].

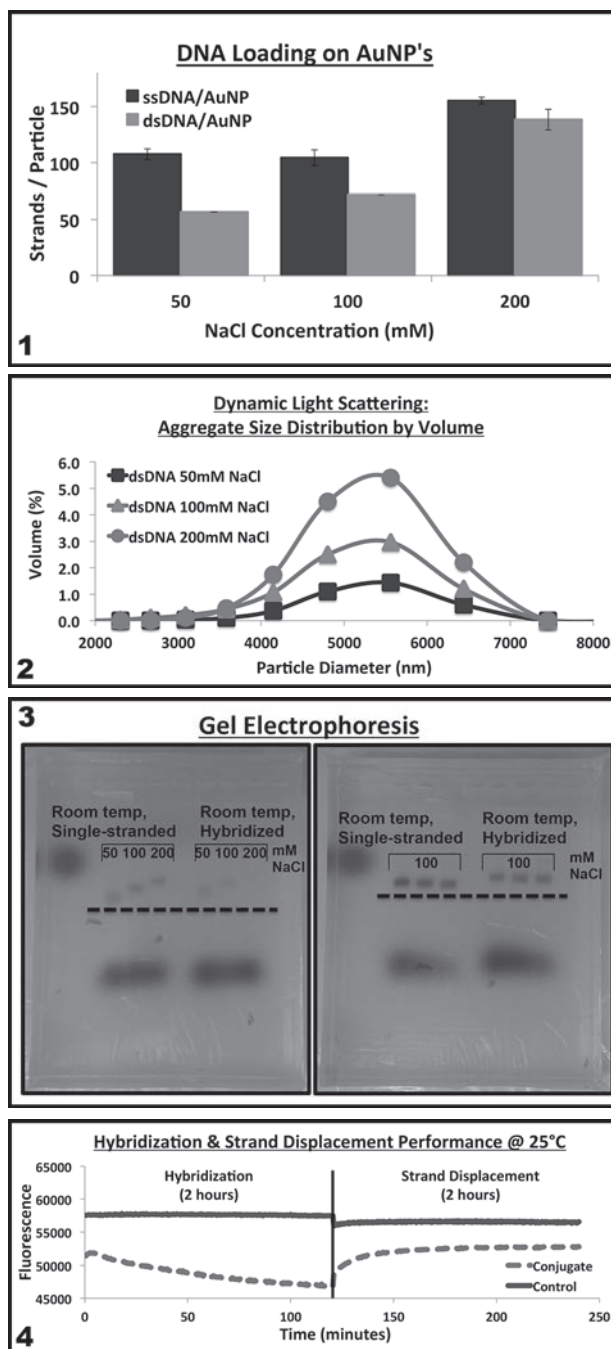


**Figure 1:** Single- and double-stranded DNA loading on AuNP surface, estimated from UV-Vis absorbance measurements.

**Figure 2:** DLS measurements in aggregate size range; dsDNA refers to hybridized DNA on conjugate surface. **Figure 3:** Gel electrophoresis for varying salt concentration trial (left) and same salt concentration trial (right). **Figure 4:** Fluorometer measurements during hybridization and strand displacement.

## References:

- [1] DeLong, R. K., et al. (2010). *NS&A*, 3(1), 53-63.
- [2] Baer, D. R., et al. (2010). *An.&Bio.Chem.* 396(3), 983-1002.
- [3] Lee, C.-Y., et al. (2007). *J. of the ACS*, 129(30), 9429-9438.
- [4] Turkevich, J., et al. (1951). *Discussions of the Faraday Soc.* (11), 55.
- [5] Demers, L. M., et al. (2000). *Analytical Chemistry*, 72(22), 5535-41.
- [6] Zhang, D. Y., et al. (2009). *J. of the ACS*, 131(47), 17303-14.

# Optimization of a Capacitive Sensing Organic Electrochemical Transistor Immunoassay

Lucy Hu

Bioengineering, University of California, Berkeley

**NNIN iREU Site: Centre Microélectronique de Provence, École Nationale Supérieure des Mines de Saint-Étienne, France**

*NNIN iREU Principal Investigator: Dr. Roisin Owens, Bioelectronics, École Nationale Supérieure des Mines de Saint-Étienne, France*

*NNIN iREU Mentor: Anna-Maria Pappa, Department of Bioelectronics, École Nationale Supérieure des Mines de Saint-Étienne, France*

*Contact: lucyhu@berkeley.edu, owens@emse.fr, anna-maria.pappa@emse.fr*

## Introduction:

The development of fast, accurate and sensitive immunoassays is of major importance for the early detection of several diseases. Traditional methods, such as the ELISA and Western Blot, operate on the time scale of hours to days; we thus aim to integrate organic electrochemical transistor (OECT) arrays with traditional immunoassays to provide both the molecular specificity of an immunoassay and the speed of a microelectronic system. Previous work in this field has been based on the integration of external enzymes [1] or on complex fabrication methods[2]. We herein present initial results of a simple capacitive OECT sensing platform for direct immunodetection.

The sensing principle was based on the capacitive change caused by the antigen-antibody affinity binding to the biofunctionalized poly(3,4-ethylenedioxythiophene) polystyrene sulfonate (PEDOT:PSS) transistor channel. When molecules are immobilized onto the channel, they add a resistive and capacitive element to the equivalent circuit of the OECT. Accordingly, the impedance changes due to the added mass to the channel, and a complex combination of the induced electrostatic charges of the added molecules is reflected in a shift in

the transconductance. A schematic representation of the OECT along with a the simplified equivalent circuit, and the transistor characteristic curves depicted in Figure 1.

## Experimental Methods:

Gold electrodes were patterned onto glass slides via photolithography and chemical vapor deposition. A layer of Parylene-C was also deposited through vapor deposition, followed by a layer of 2% MicroClean soap solution followed by a sacrificial layer of Parylene-C. The last part of the fabrication process involved the development of photolithographically patterned channels, the dimensions of which were  $10 \times 10 \mu\text{m}^2$ . Finally, the (semi)conducting solution was spin-coated to the channel, and the gate that were exposed via reactive ion etching.

In order to introduce hydroxyl groups onto the transistor channel, a PEDOT:PSS:polyvinyl alcohol (PVA) blended solution was used as the active solution [3]. Following, the channel was further functionalized and treated with a (3-glycidyloxypropyl) trimethoxysilane (GOPS) solution in order to introduce epoxy groups on top of the channel and thus allow protein immobilization.

Initially, in order to standardize our OECT based immunoassay, a model system was employed, consisting of a primary and a secondary (fluorescent) antibody. The primary antibody was primarily immobilized onto the epoxy-modified transistor channel, and a bovine serum albumin (BSA) solution was deposited prior to the immobilization of the secondary antibody, in order to avoid unspecific binding. All the aforementioned steps, including the biofunctionalization of the channel are schematically represented in Figure 2.

## Results and Discussion:

We herein fabricated PEDOT:PSS-based OECT towards the development of an immunosensing platform, Initially our work involved the study of, different biofunctionalization methodologies. It was found that the thicker the GOPS layer onto the transistor channel, the higher the standard

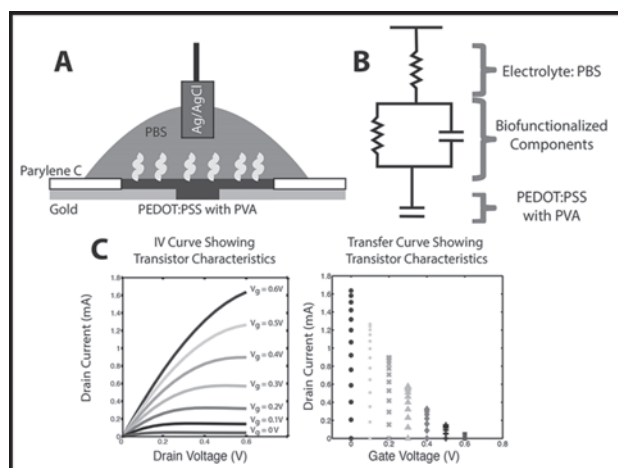


Figure 1: A) Schematic representation of the OECT. B) design of a simplified equivalent circuit. C) Steady state characteristics: output and transfer curves of the fabricated OECTs

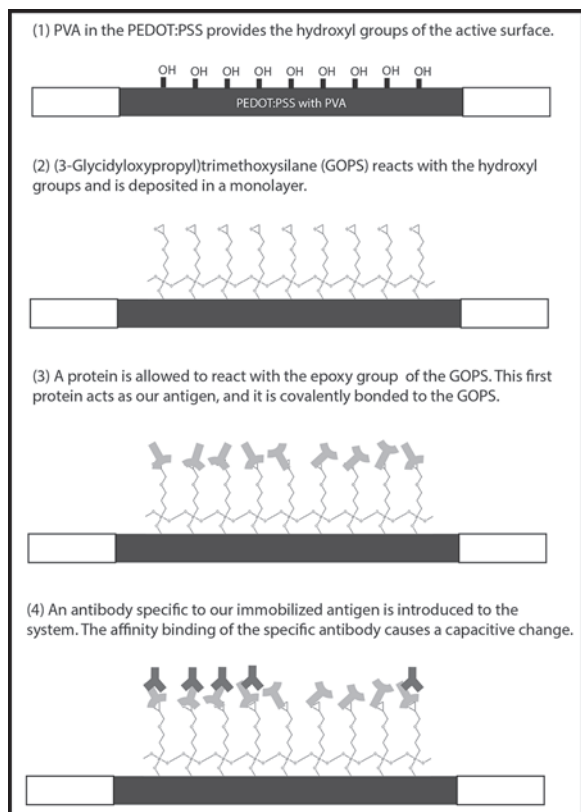


Figure 2: Biofunctionalization concept diagram.

deviations were observed leading to less consistent data, thus indicating the necessity of developing a GOPS mono-layer deposition method. The biofunctionalization methodology was validated by checking the fluorescence of the device after the immobilization of the secondary antibody.

Additionally, we studied the effect of the electrolyte (PBS) concentration on the transconductance cut-off frequency. It was found that the transconductance cutoff frequency decreases as the PBS concentration decreases, due to the electrolyte's equivalent resistance in the equivalent circuit. Given that the theoretical transconductance cutoff is dependent on the combined impedance of all the elements in the circuit and in order to be able to sense small changes in impedance, the OECTs were tested after each critical immobilization step with varying PBS concentrations (i.e., 1X, 0.1X, 0.01X, and 0.001X). Those results are graphed and shown Figure 3. Ultimately, none of the higher electrolyte concentrations (1X, 0.01X, and 0.01X) show clear shifts between steps in the biofunctionalization procedure; the trendlines have large error bars that all overlap giving null results. The OECT tested under PBS 0.001X, however, shows promising results, as there are clear, distinguishable transconductance shifts for

the covalent bonding of GOPS to the channel and for the covalent bonding of the first antibody to the GOPS. The lack of shift in subsequent steps for the PBS 0.001X sample makes sense if the secondary antibody is not binding or is currently too small to detect. To validate that the normalized shifted curves are an accurate representation of the transconductance cutoff relationship, the derivative functions were graphed and yielded the same results as the visual shifts.

These results indicate that the capacitive method can successfully detect covalent bonding onto the transistor channel.

### Future Work:

The next step of this work is to successfully detect the antigen-antibody affinity binding via a transconductance shift. We plan to improve the biofunctionalization process by focusing on the GOPS monolayer formation onto the transistor channel, since variations in a thick GOPS layer interfere creates noise in the transconductance that obscures the desired shift. Moreover specific disease detection models will be also studied.

### Acknowledgements:

The authors acknowledge support from the Department of Bioelectronics at the École Nationale Supérieure des Mines de Saint-Étienne, the National Nanotechnology Infrastructure Network International Research Experience for Undergraduates (NNIN iREU) Program, and the National Science Foundation, Grant No. ECCS-0335765.

### References:

- [1] B. Kavosi, et al., Biosens. Bioelectron. 74, 915-923 (2015).
- [2] W. T. Li, et al., J. Biomed. Nanotechnol. 11, 2050-2056 (2015).
- [3] X. Strakosas, et al., J. Mater. Chem. B. 2, 2537-2545 (2014).

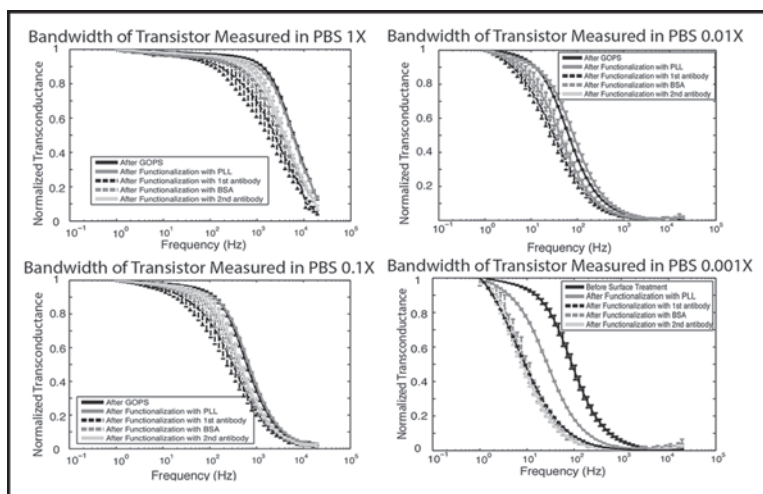


Figure 3: Frequency dependence of the transconductance in varying PBS concentrations between all the critical immobilization steps.

# The Wrinkling of Thin Elastic Membranes as a Cancer Diagnostic

**Adam Kunesh**

**Physics and Mathematics, University of North Carolina at Chapel Hill**

**NNIN REU Site: ASU NanoFab, Arizona State University, Tempe, AZ**

*NNIN REU Principal Investigator: Junseok Chae, School of Electrical, Computer, and Energy Engineering (ECEE), Arizona State University*

*NNIN REU Mentor: Jennie Appel (2010 NNIN REU at Arizona State University), ECEE, Arizona State University*

*Contact: apkunesh@live.unc.edu, junseok.chae@asu.edu, appeljh@tigermail.auburn.edu*

## Abstract:

Cancerous cells generate wrinkles on sufficiently thin elastic membranes. Exploiting this phenomenon could enable the fabrication of a point-of-care bladder cancer diagnostic device. Historically, there has been difficulty producing thin, large membranes; while this remains a difficulty, a limited number of membranes were fabricated. Membranes as thin as 150 nanometers were produced. The wrinkles generated by bladder cancer cells, large enough to be observed under optical microscope, were characterized for each of these membranes.

## Introduction:

Cell locomotion is dependent on the forces a cell exerts on its exterior environment, called cell traction forces. When this exterior environment is composed of an ultra-thin elastic membrane, these traction forces result in significant wrinkling of the surrounding membrane. As a cell attempts to move, it inadvertently draws the ultra-thin membrane towards localized focal points at the outer edge of the cell membrane, and the angular component of the stress in the surrounding membrane becomes negative. This angular compression results in a localized buckling of the membrane.

Because cancer cells produce distinctly different forces from healthy cells [1], this wrinkling phenomenon could be applied as a point-of-care cancer diagnostic device. One of the great strengths of such a device is that a heterogeneous sample of cells might be used for reliable diagnosis of cancer; for example, the cells found in urine samples could be used to diagnose bladder cancer.

Attempts to find a quantifiably testable predictor for the formation of wrinkles yielded a numerical study [2]. Fitting curves to the simulated data yielded equations predicting length and number of wrinkles based on the physical qualities of the membrane (radius, thickness,

Poisson's Ratio, residual stress) and those of the cell (radius, force exerted by a half-cell). These equations are found in Figure 1, with  $R^*$  as the wrinkle length,  $N$  the number of wrinkles,  $\delta_c$  the critical membrane displacement for wrinkle formation (linearly related to idealized cell traction force),  $R$  the membrane radius,  $r_0$  the cell radius,  $\beta$  the distance pulled at the boundary of the membrane (linearly related to residual stress),  $h$  membrane thickness, and  $\sigma$  Poisson's Ratio.

## Experimental Procedure:

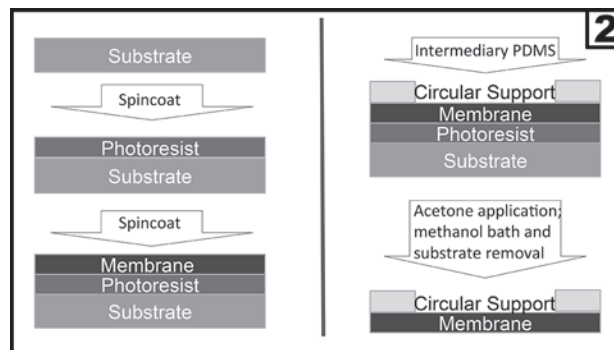
The membrane fabrication process is summarized in Figure 2. First, several microns of AZ 4330 photoresist were spun onto a 4-inch silicon wafer. After baking for one minute at 100°C, we placed hexane-diluted polydimethylsiloxane (PDMS) on top of the photoresist and again spun the sample, this time at 6000 rpm for three minutes. At this point, our sample was placed on a hot plate at 80°C for 16-18 hours.

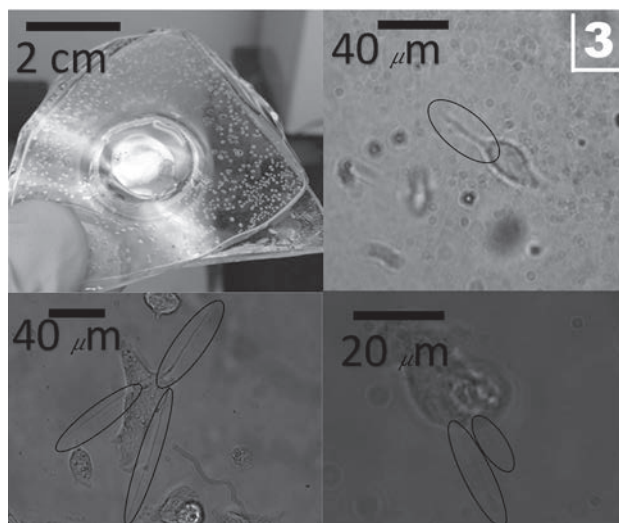
After the PDMS membrane cured, a thick PDMS support structure was adhered to the sample via intermediary

$$R^* = \sqrt{\frac{1 - \sigma \delta R + \beta r_0}{1 + \sigma \delta r_0 + \beta R} R r_0} \quad [1]$$

$$N = 3/2500 \beta r_0 / h^2 + 69/400 r_0 / h + 1/50 \beta / h + 2$$

$$\delta_c = \frac{23}{20} \beta - \frac{1}{250} \frac{r_0 \beta}{h} + \frac{131}{5} \frac{h^{5/3}}{r^{2/3}} + \frac{56}{10} h - \frac{19}{20} \ln\left(\frac{r_0}{h}\right)$$





PDMS layer and cured at 100°C for two hours. After cooling, the sample was treated with an acetone mist via spray bottle and subsequently immersed in a methanol bath. Careful peeling of the support structure resulted in the production of a bounded membrane, which could be seen to oscillate in the methanol. The membrane was then carefully removed from the methanol bath [3].

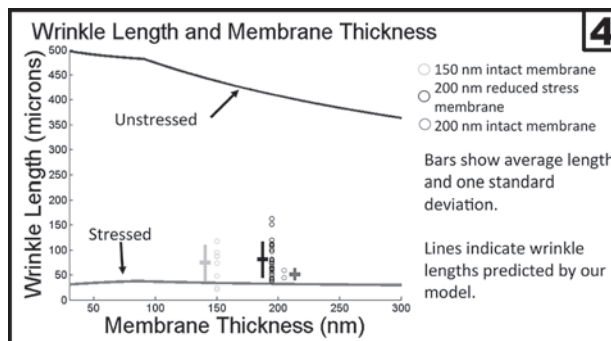
T24 bladder cancer cells were cultured. The cells were incubated on the membrane at 37°C in 5% CO<sub>2</sub> for 24 hours. Over this time period, cells adhered to the surface and contracted, creating the wrinkles observed via inverted microscope (Figure 3).

### Results and Conclusions:

Five membranes were fabricated: 1 × 150 nm, 3 × 200 nm, and 1 × 300 nm. Membranes of each thickness were tested and T24 cells were unable to generate wrinkles in the 300 nm membrane. The length and number of wrinkles formed on the 150 nm, 200 nm, and 200 nm reduced-stress membrane after 24 hours were 70±35 microns and eight; 52±10 microns and two; and 82±33 microns and twenty-nine, respectively. After 48 hours, these quantities were: 40±27 microns and thirteen; 40±7 microns and two; and 85±54 microns and 26. The 24 hour data is summarized in Figure 4.

The reduced-stress membrane was a 200 nm membrane with hole in the center (roughly a quarter of the area of the membrane). This hole allowed the membrane to relax and relieve some of its residual stress, which likely accounts for the substantial increase in both length and number of observed wrinkles.

We were unable to reduce the membrane thickness below 150 nm. Although membranes as thin as 125 nm were observed in the methanol environment, removal of the membrane from the bath caused breakage.



While we did find an upward trend in length and number of wrinkles as membrane thickness was reduced, our results indicated that our membrane was stressed as a side effect of our fabrication process. This residual stress substantially increased the minimum force required for cells to generate wrinkles, and likely reduces the device's power to differentiate between cells producing different ranges of force.

### Future Work:

In the future, we hope to refine our fabrication process to increase control over the residual membrane stress and thickness while improving membrane stability. This will allow for the statistical analysis of wrinkle formation by a variety of cells and an optimization of membrane characteristics for the fabrication of a point-of-care bladder cancer diagnostic device.

### Acknowledgments:

Many thanks to my PI, Dr. Junseok Chae, and my mentor Jennie Appel for all of their guidance and assistance. Thanks also to the National Nanotechnology Infrastructure Network Research Experience for Undergraduates (NNIN REU) Program and to the National Science Foundation for enabling my research under Grant No. ECCS-0335765. Dr. Trevor Thornton and the CSSER staff at ASU were instrumental to my learning and my experience. Finally, thanks to my fellow interns (Raul Flores, Alex Rosner, and Abby Magee) for providing a sounding board and a source of entertainment.

### References:

- [1] Li, et al., Quantifying the Traction Force of a Single Cell by Aligned Silicon Nanowire Array, *Nano Letters*. 2009: 9, No. 10, 3575-3580. DOI: [10.1021/nl901774m].
- [2] Geminard, et al., Wrinkle formations in axi-symmetrically stretched membranes, *Eur. Phys. J. E*. 2004: 15, 117-126 [DOI: 10.1140/epje/i2004-1004101].
- [3] Kang, et al., Large-Scale, Ultrapliable, and Free-Standing Nanomembranes, *Adv. Mater.* 2013: 25, 2167-2173 [DOI: 10.1002/adma.201204619].

# Fabrication and Design of EGFET Devices for Biosensing

**Abigail Magee**

**Biomedical Engineering, University of Central Oklahoma**

**NNIN REU Site: ASU NanoFab, CSSER Facility, Arizona State University, Tempe, AZ**

*NNIN REU Principal Investigator: Jennifer Blain Christen, Electrical Engineering, Arizona State University, Tempe, AZ*

*NNIN REU Mentor: Uwa Obahiagbon, Electrical Engineering, Arizona State University, Tempe, AZ*

*Contact: amagee@uco.edu, jennifer.blainchristen@asu.edu, uwa@asu.edu*

## Abstract:

Ion-sensitive field effect transistors (ISFET) measure the presence of ions in a solution via their effect on current flow within the device. The ions induce charge in the device via capacitive coupling from the ion-sensitive membrane. The extended gate field effect transistor (EGFET) is a modified version of the ISFET that uses low cost FET transistors combined with a sensing membrane and reference electrode structure fabricated separately. This structure requires fewer fabrication steps and enables flexibility and adaptability in application. The EGFET is more suitable for continuous monitoring in harsh environments, since the sensing area is external to the transistor. While the EGFET's sensing area is physically remote, the principles of operation remain the same. This project focused on design and fabrication of EGFETs with different sensing membranes and geometries. The systematic investigation of the device parameters enables informed designs for increased sensitivity to pH. The devices were fabricated with chrome/gold reference electrodes and either a silicon nitride or silicon dioxide sensing membrane. The devices were tested with pH buffer solutions to provide consistent pH samples. Initial testing determined the silicon nitride layer had poor quality, with pinholes and cracks evident when surface features were analyzed with an optical profilometer, resulting in poor characterization and etching of the electrode.

## Introduction:

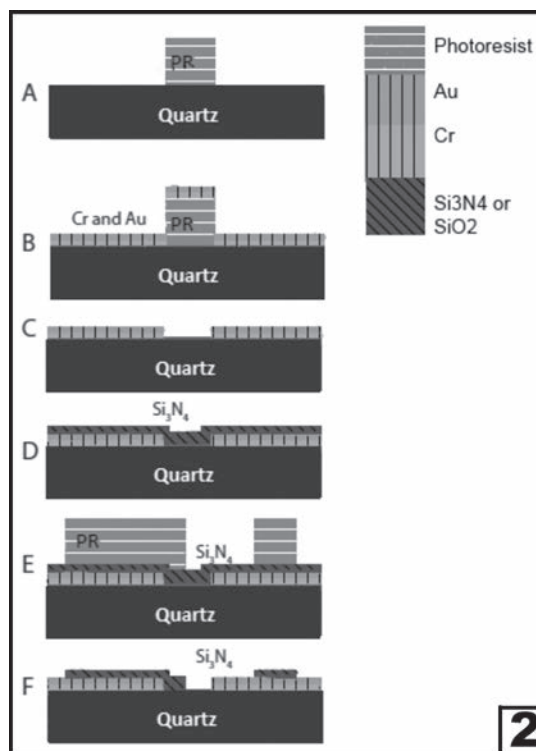
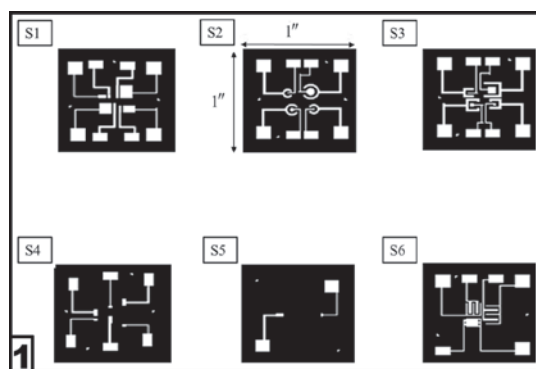
Many sensors rely on pH in order to detect a change in a system and adjust pH or trigger another response. As an environmental sensor, EGFETs could be used to track pH changes in water to determine if there is contamination. In biological or biomolecule applications, EGFETs can be used to detect pathogens, antibodies, or proteins; they can also track pH levels for cultured cells.

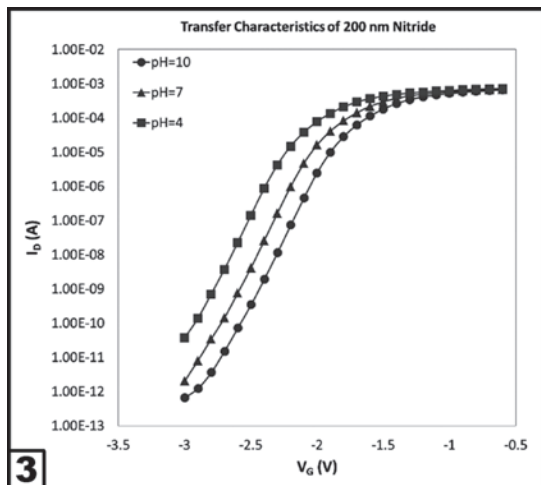
Increasing sensitivity of the device would increase the ability of the device to distinguish between minute pH changes in an electrolyte or pH changes due to biomolecules bound to its surface. This research project investigates several geometric and spacing variations to optimize for pH sensitivity.

## Experimental Procedure:

**Fabrication of the Biosensor.** The masks for the fabrication steps were designed using L-Edit, as shown in Figure 1. The designs were printed on a Mylar film using a 25,400 dpi printer, attached to a soda-lime glass substrate, and used in the photolithography steps. Positive photoresist was used for photolithography.

The fabrication of the devices followed the process shown in Figure 2. An adhesion layer of 10 nm chromium was deposited





followed by 170 nm of gold; both were deposited using evaporation. The thickness of nitride or oxide deposition was intentionally varied between the sets. Sets 2, 3, and 4 had 200 nm of silicon nitride, 400 nm of silicon nitride, and 200 nm of silicon dioxide, respectively. For the set that contained oxide rather than nitride, the process followed the same format as in the previous sets; the nitride was simply replaced with silicon dioxide.

**Setup for Experimentation.** Wires were attached to the contact pads of the sensors using a silver-based conductive epoxy. A centrifuge tube, with a section cut off from the tip, was used in packaging the device by creating a confinement for the electrolyte. The centrifuge tube was bonded to the quartz substrate using a marine-grade epoxy, exposing the sensing areas so that the solutions used would be in contact with the correct locations on the device. The devices were exposed to an electrolyte for 24 hours without taking any measurements, allowing the interfaces and surfaces to reach a steady state.

**Data Acquisition.** In order to measure the pH values versus the voltage, we used a program in MATLAB in order to automate the measurements to determine this relationship. A Keithley source meter was also used for data acquisition purposes with TSP Express.

The devices were measured using buffer and titrated solutions. Once the solution was added to the device, we waited five minutes to start the program. A computer program was run for five sweeps and the device was reset within the first sweep. The sweeps were set up with a  $V_{GS}$  of -3.5V to -0.5V, a  $V_D$  of 0.2V and 0.5V, and a step size of 0.05V. Transfer and output characteristics were plotted in Excel and analyzed once data acquisition was complete.

**Results:**

During initial testing, it was observed that the nitride and the gold electrodes were being etched due to poor quality of the nitride layer. This affected the characterization,

Sensor	Area/Spacing	pH Sensitivity
	12mm <sup>2</sup>	49.97 mV/pH
	3.14mm <sup>2</sup>	50.39 mV/pH
	4mm <sup>2</sup>	49.98 mV/pH
	1mm	49.98 mV/pH
	11mm	49.99 mV/pH
	1mm	49.98 mV/pH

because the transistor and program picked up the etching mechanism rather than just the pH reaction.

The devices with the improved sensing membranes had no visible etching with the new buffer solutions. Transfer characteristics of these corrected devices had the expected pH sensitivities, as in Figure 3. Details concerning the pH sensitivity of the devices are shown in Figure 4.

**Conclusions:**

The results from testing in Figure 4 indicate the devices have the sensitivities expected. These results are not final, as more testing is needed to confirm these results. However, the current results demonstrate the devices are working as expected and could be used in further testing to determine a difference in pH sensitivity in relation to geometry, spacing, and surface area.

In the future, a better PECVD process will need to be used so the sensing membrane is deposited more evenly and with fewer defects. This would improve the characterization of the devices due to the elimination of etching processes. It would also prove beneficial to fabricate devices with different geometric structures, but with the same area, in order to compare the effect of geometry and spacing on pH sensitivity more effectively and with fewer compounding factors.

**Acknowledgements:**

Many thanks to Dr. Jennifer Blain Christen and my mentor, Uwa Obahiagbon for helping me with this research and giving me the opportunity to work in their lab. Thanks to the CSSER staff at Arizona State University for being available to help with the fabrication process and to my fellow interns. Thanks to the NNIN REU Program and to the National Science Foundation, Grant No. ECCS-0335765, for giving me this opportunity.

# Influence of Cell Spreading Area on Uptake of Gold Nanoparticles

**Adriana Mulero**

**Chemical Engineering, University of Puerto Rico-Mayaguez**

**NNIN iREU Site: National Institute for Materials Science (NIMS), Tsukuba, Ibaraki, Japan**

*NNIN iREU Principal Investigator: Dr. Guoping Chen, Tissue Regeneration Materials Unit, National Institute for Material Science*

*NNIN iREU Mentor: Xinlong Wang, Tissue Regeneration Materials Unit, National Institute for Material Science*

*Contact: adriana.mulero1@upr.edu, guoping.chen@nims.go.jp, wang.xinlong@nims.go.jp*

## Abstract:

Nanoparticles (NPs) have been proved to be a promising material for drug delivery, cancer therapy, and bioimaging. However, there is growing concern about their cytotoxicity, which may cause an inverse effect on human health. In order to develop safer and efficient NPs, people need to fully understand how cells react with the NPs. Previous studies investigated the influence of NPs properties on cellular uptake. However, little attention was paid to understand the influence of cell membrane tension on the uptake. Micropatterns were used to control the membrane's tension on single cell scale; the greater the spreading area, the greater the tension on the cell membrane [1]. Thus in this study, a series of microdots with various diameters (20, 40, 60, and 80  $\mu\text{m}$ ) were developed using photolithography techniques. Gold nanoparticles (AuNPs) with sizes of 50 nm were synthesized following the Turkevich method and coated with FITC labeled PEG. Mesenchymal stem cells (MSCs) were cultured on the micropatterns and treated with FITC-PEG-AuNP to investigate the influence of cell spreading area on uptake of NPs. The results indicate that PEG-coated AuNP are non-toxic to the MSCs. Patterned cells with different spreading areas and cellular tension can uptake the FITC-PEG AuNPs.

## Introduction:

Nanoparticles (NPs) have been found to be a promising way for visualizing specific cell types, delivering drugs directly into the cell, and cancer therapies. For all these applications to be successful, it is important to study the NPs and cell interaction, including cellular uptake and cellular toxicity. Endocytosis is the mechanism that cells use to bring the nutrients and NPs into the cell. The cellular membrane bends forming a vesicle, providing them transportation into the cell. Previous studies [1] have analyzed NPs properties and their effects on the uptake. However, little attention was paid to understand how the cellular membrane properties influence the cellular uptake. These include the cellular membrane tension affecting the membrane's capacity to bend to form the vesicles.

Micropatterns have been proved to efficiently control the cellular membrane tension on a single cell scale; the greater the spreading area, the greater the tension on the membrane [2]. In this project, we evaluated how the cellular membrane tension, of mesenchymal stem cells (MSCs), controlled by micropatterns of different size dots affects the uptake of gold nanoparticles (AuNP).

## Experimental Procedure:

**Micropatterning Process.** By using photolithography techniques, the micropatterns were developed on a transparent polystyrene square surface (6.25  $\text{cm}^2$ )

cut from a tissue culture dish, which supported cell adhesion. Poly(vinyl alcohol) (0.3 mg/mL) was used as the photoreactive solution. The design consisted of dots with diameters of 20, 40, 60, and 80  $\mu\text{m}$ . The micropatterned surfaces were characterized using atomic force microscopy.

**AuNP Synthesis.** Following the Turkevich method, we synthesized the 50 nm sphere AuNP [3] using 0.01% chloroauric acid ( $\text{HAuCl}_4$ ) and 1% tri-sodium citrate solution as the reduction solution. The synthesis was kept at constant stirring and a temperature of 110°C. It was later ultrasonicated to disperse the molecules before the surface modification. The mPEG-SH and the FITC-PEG-SH were added to AuNP solution at a 3:2 ratio. The mix was stirred overnight to obtain the FITC-PEG modified AuNP.

**Cell Experiments.** The cell experiments were divided into two groups: flat and patterned surface. For the flat surface, we seeded the cells on a 96-well-plate with a cell density of 1,000 cells/well. For the patterned surface, the micropatterns were sterilized with ethanol and water, then placed one square per well on a six-well-plate; cell density 5,000 cells/well. After the cells attached, the previous medium was aspirated and the growth medium containing the AuNPs was added to the cells. They were treated with 0.1, 0.5, 1 and 3 nM FITC-PEG AuNP concentrations. The cells were then tested for cell viability with WST-1, and cellular uptake studied with fluorescence microscope.

## Results and Conclusions:

Micropatterns were characterized to measure the diameter and depth of each pattern. Patterns were proved to go according to the design, with a depth around 60 nm (Figure 1). Nanoparticles were characterized with scanning and transmission electron microscope to analyze their shape and size distribution (Figure 2). Size was proved to be spherical, and from the increase in size, we said that FITC-PEG layer was successfully added. Cell viability test (WST-1), was performed 6, 12, and 24 hours post-seeding. The WST-1 results showed no statistical difference between the NPs treated group and the control group (Figure 3). For the NPs uptake (Figure 4), cells were examined under the fluorescence microscope to view the NPs fluorescence due to the FITC modification.

On the bright field, the NPs were observed with a red color, pointed with arrows. Whenever the NPs were aggregated, the green fluorescence intensity increases. The nucleus, stained blue, showed there was one cell per dot. There is green fluorescence inside the contour of the cell every size dot, suggesting there are NPs inside the cells.

We concluded the following. First, the FITC-PEG AuNP was non-toxic to MSCs, and they presented a promising way to visualize cellular uptake. Second, the patterned cells with different spreading areas, and cellular tension could uptake FITC-PEG AuNPs. Future work includes quantifying the fluorescence intensity to obtain quantitative NPs uptake results and visualizing the NPs distribution inside cells using laser confocal microscope.

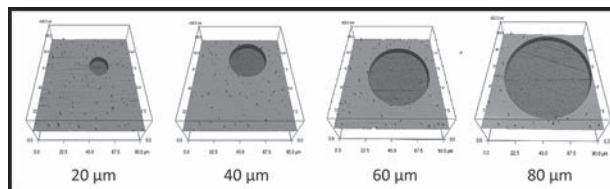


Figure 1: Micropatterns, 3D view of the different size dots.

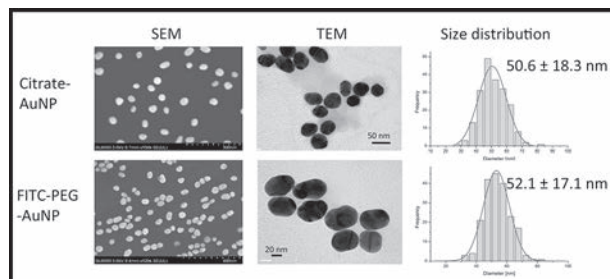


Figure 2: Gold nanoparticles shape and size characterization.

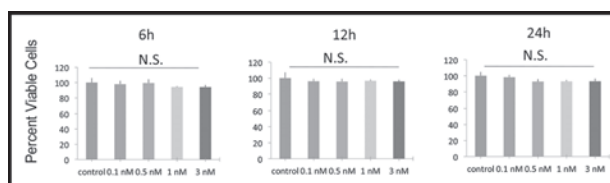


Figure 3: Cell viability test or measurement of the NP toxicity to cells.

## Acknowledgements:

I want to thank my mentor Wang for all his support, Professor Chen for his guidance, the National Nanotechnology Infrastructure Network International Research Experience for Undergraduates (NNIN iREU) Program, National Institute for Materials Science, Japan, and National Science Foundation (under Grant No. ECCS-0335765). Also a very special thank you to Dr. Lynn Rathbun and Dr. Nancy Healy for coordinating the iREU Program.

## References:

- [1] ACS Nano, 7, 1961, 2013. J. Colloid Interface Sci., 438, 68, 2015. Biomaterials, 54, 226, 2015.
- [2] Biophysical Journal, 94, 4984, 2008.
- [3] Environmental Toxicology and Chemistry, 33, 481, 2014.

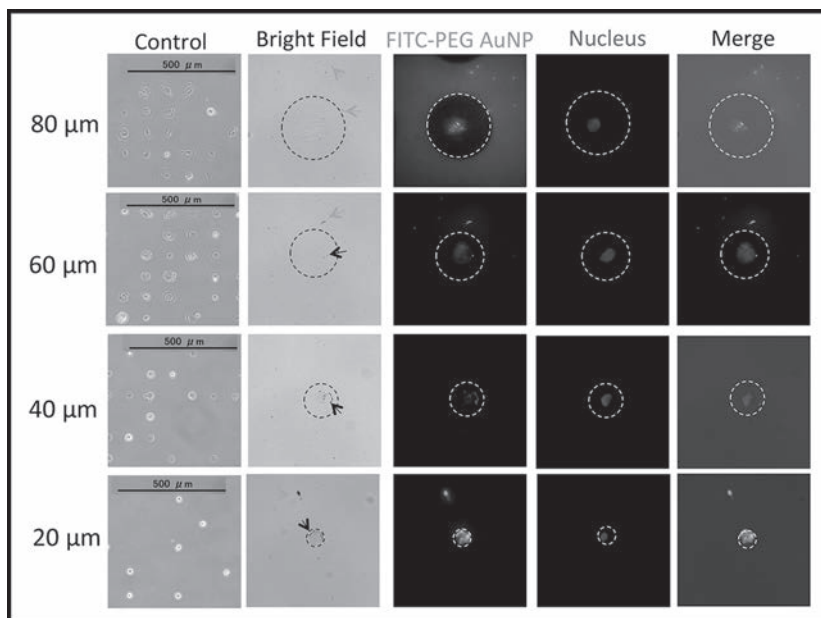


Figure 4: NP uptake test on patterned surface examined under fluorescence microscope.

# Nanoplasmonic Biosensing Microfluidics for Immune Status Monitoring of Critically-Ill Children

**Taylor Pauls**

**Biomedical Engineering and Physics, University of Arkansas**

**NNIN REU Site: Lurie Nanofabrication Facility, University of Michigan, Ann Arbor, MI**

*NNIN REU Principal Investigator: Dr. Katsuo Kurabayashi, Mechanical Engineering, EE and CS, University of Michigan*

*NNIN REU Mentor: Dr. Robert Nidetz, Mechanical Engineering, University of Michigan*

*Contact: tpauls@uark.edu, katsuo@umich.edu, nidetz@umich.edu*

## Introduction:

The availability of a real time immune system monitoring system can be extremely useful in the laboratory and has potential clinical uses. The current standard for monitoring is an enzyme-linked immunosorbent assay (ELISA), which takes 1-2 days and requires large amounts of sample in comparison to a microfluidic system. Using a microfluidic system that can detect and monitor the activity of immune system in real time has many promising applications. Monitoring specific cytokines, which are proteins expressed from white blood cells that are triggered, and trigger the immune system, provides information as to the current state of the immune system. Information gathered from the microfluidic assay based on the cytokines can aid physicians to determine the best possible treatment and can have near immediate updates of the patient's state. This can prove extremely useful in immune-status updates pre-and post-operation, as well as a system of monitoring during an infection or disease. Single cell capture enables studying the most basic unit of our bodies and can potentially transform treatment and understanding of diseases.

Recently, the Fu group incorporated micropipette aspiration as a mechanism to study the mechanical differences of cancerous versus non-cancerous cells and the consequences for future cancer treatments [1].

The device proposed here aims to capture single cells to monitor their isolated behavior for relevant time periods for critical immune status updates. The microfluidic device consists of distinct chambers for single cell capture (see Figure 1). A cross-linked, biocompatible, synthetic polymer, polyethylene glycol (PEG-gel), will be patterned on top of the chambers to enable cell capture. In conjunction with the PEG-gel pattern, the previously developed technology of localized surface plasmonic resonance (LSPR) of gold nanorods can be implemented for biosensing secreted proteins [2].

## Experimental Procedures:

**CAD and Device Fabrication.** K-layout was used for the design of the microfluidic device. Two designs were ultimately used in our process. The first design consisted of an inlet, outlet, and three arrays of cell capture chambers throughout the channel, varying with different sizes of the chambers per device, see Figure 1. A silicon wafer was fabricated following the device design (Figure 2) using standard DRIE procedures. The second design consisted of holes displaced relative to the center of the cell capture chambers in the first design, which was used to pattern PEG-gel.

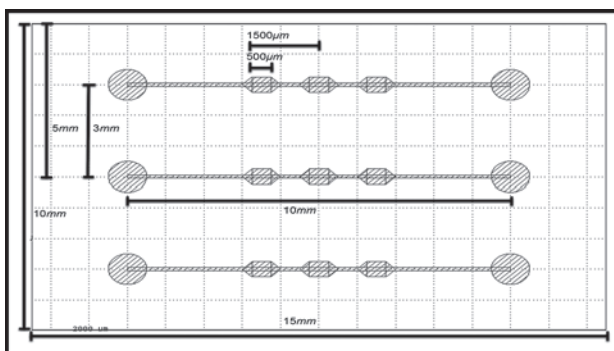


Figure 1: A CAD drawing of the device design that is used for PDMS molding. Dimensions not listed are; channel width of 100 µm, and channel depth of 50 µm. Each channel has three cell capturing wells.

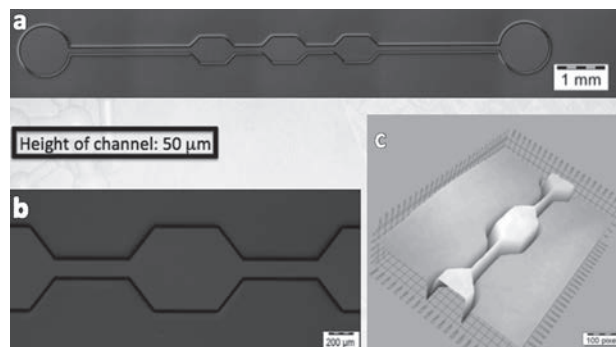


Figure 2: Images of the fabricated silicon wafer. (a) Entire channel. (b) Cell capture chamber. (c) 3-D image of (b) to show topography.

**Soft Lithography.** PDMS and glass substrates were activated via oxygen plasma treatments prior to silanization. Polyethylene glycol diacrylate, MW 575 g/mol, was spun on the samples and exposed over the mask via UV-light for 2-3 seconds. After development by deionized water, the samples were dried by nitrogen gun.

**Cell Capture.** Human T-Helper cells (THP-1) were used in conjugate with CD14 primary antibody. First, the antibody was deposited and dried onto the features. After a sufficient drying time, at least 30 minutes, a PDMS microchannel was placed over the features and THP-1 cells concentrated to  $10^5$  cells/mL are flown through the channel. Approximately every ten minutes, for 30 minutes, 10 ml of cells were manually pumped via micropipetting, see Figure 3.

**Data Acquisition.** All cell capture experiments were performed with a Nikon Eclipse Ti-S microscope under brightfield view. Fabrication images were taken by an Olympus BX-51 microscope under bright view.

### Results and Conclusions:

Soft lithography and cell capture proved successful on both PDMS and glass samples, but poor surface adhesion of PEG-gel onto PDMS substrates limited PDMS patterned PEG-gel experiments. Varying the exposure time, oxygen plasma treatments, silanization baths, and development times with PDMS patterning did not substantially improve the lithography. Swelling of the PDMS during the silanization step proved to be quite difficult to overcome for consistent or accurate patterning. Therefore, most cell capture experiments were carried out with PEG-gel features on glass slides.

However, cell capture was successful on a large area of PEG-gel on a PDMS sample. After many trial and error experiments, favorable antibody dry time coupled with sufficient cell flow exposure to the features was established. Single cell capture has not yet proved successful on the tested 50 mm diameter PEG-gel features, but double cell capture has (see Figure 4). Lithography of the 25 mm PEG-gel features have not yet been detected on the glass slide substrate.

### Future Work:

With double cell capture being possible onto the PEG features, more efforts will be employed for successful lithography onto PDMS including the use of a desiccator chamber for vapor silanization to avoid the swelling due to the solvent used. An addition, altering the cell capture design may be a possibility to improve the efficiency of cell capture on the PEG-gel features, as well as using a syringe pump to control the cell flow over the features. Employing fluorescent antibodies will prove helpful for both quantifying antibody presence on the PEG-gel features and detecting of the smaller 25 mm features.

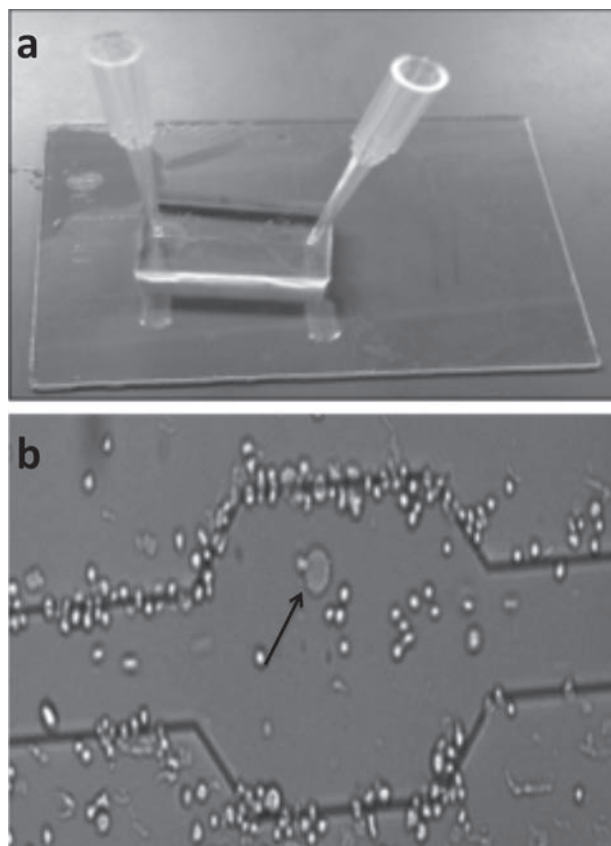


Figure 3: (a) Cell capture experimental set up. (b) Cell capture experiment, arrow pointing at PEG-feature patterned on glass.

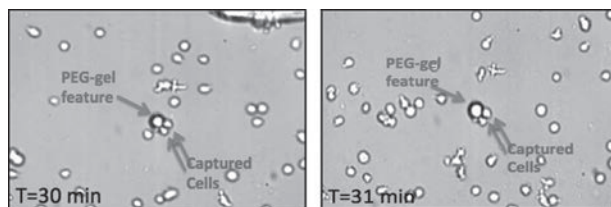


Figure 4: Time lapse demonstrates two cells captured on the PEG-gel feature after 30 and 31 minutes.

Once successful PEG-gel lithography onto PDMS and single cell capture is a reality, the sensing with LSPR AuNRs can be implemented for completion of this device.

### Acknowledgments:

I thank my PI, Dr. Katsuo Kurabayashi, my mentor, Dr. Robert Nidetz, the entire Kurabayashi lab for help and support, as well as the LNF staff, and the NNIN REU Program and the NSF (Grant #ECCS-0335765) for funding.

### References:

- [1] Lee, L. M., and Liu, A. P., J. Nanotechnol. Eng. Med. 5, 0408011-0408016 (2014).
- [2] Chen, P., et al. ACS Nano 9, 4173-4181 (2015).





# A High-Throughput Image-Processing Based Analysis of Dynamic Cell Surface Interactions in a Microfluidic Chip

**Brian Ryu**

**Chemical and Biomolecular Engineering, Johns Hopkins University**

**NNIN REU Site: Institute for Electronics and Nanotechnology, Georgia Institute of Technology, Atlanta, GA**

*NNIN REU Principal Investigator: A. Fatih Sarioglu, Electrical Engineering, Georgia Institute of Technology*

*NNIN REU Mentor: Ruxiu Liu, Bioengineering, Georgia Institute of Technology*

*Contact: bryu2@jhu.edu, sarioglu@ece.gatech.edu, rliu76@gatech.edu*

## Abstract:

Immunoaffinity-based lab-on-a-chip technologies offer high-throughput, label-free methods of cell characterization and are attractive for developing low cost point-of-care devices for cellular diagnostics. A biologically functionalized microfluidic channel would allow for detection of cells of particular interest, such as cancer cells as different cells have varying levels of affinity for different antibodies. This project focused on the development of an image-based analysis method combined with a microfluidic platform to identify cells using surface affinities of plasma membranes. A microfluidic channel was designed and constructed with polydimethylsiloxane (PDMS) using soft lithography. The channel was partially functionalized with different coatings including poly-L-lysine (PLL), a positively charged amino acid polymer that electrostatically attracts the negatively charged plasma membrane of cells. It was predicted that the cells would slow down as they traverse the coated region due to the electrostatic attraction. The motion of cell population traversing the channel was captured before and after they reach the PLL-coated region using a high-speed camera. A custom image processing software was developed to analyze and compare average velocity profiles of cells and neutral particles that are similar in size. The developed platform can be used to study the dynamics of immunoaffinity-based cell capture in microfluidic devices.

## Experimental Procedure:

**Microfluidic Device Design and Fabrication.** The microfluidic device was designed in the form of a serpentine channel with an inlet and an outlet at respective ends to maximize the channel length. The serpentine microfluidic channel was 34  $\mu\text{m}$  high, 1.4 mm wide, and 1.9 m long. The length of the channel ensures that cells sediment and reach a steady state on the floor of the channel before they interact with the coated region. The sedimentation process was modeled using Stokes flow [1], assuming a cell density ( $\rho_c$ ) of 1.05  $\text{g}/\text{cm}^3$  and a fluid density ( $\rho_f$ ) of 0.996  $\text{g}/\text{cm}^3$ . The calculated sedimentation velocity was 7.6  $\mu\text{m}/\text{s}$ . Therefore, the time required for all cells to sediment was approximated to be 5 s, which is much shorter than the time cells spend in the microfluidic channel during our experiments.

The device was fabricated using soft lithography (Figure 1). SU-8 negative photoresist was spun on a 4-inch silicon wafer and was patterned using standard photolithography to create a mold. The fabricated mold was inspected using a Dektak 150 profilometer to ensure consistent channel height across the device.

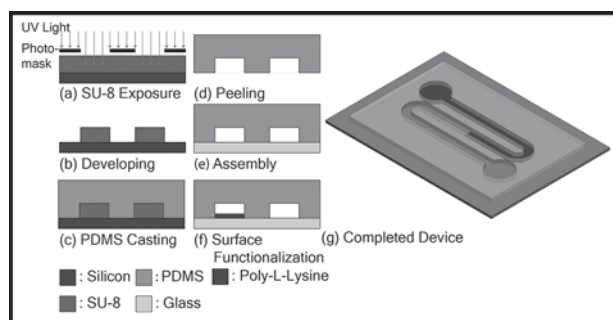


Figure 1: Overview of device fabrication process using soft lithography.

PDMS prepolymer and cross-linker (Sylgard 184) mixed at 10:1 ratio was poured on the SU-8 mold and cured for at least for four hours at 65°C. The cured PDMS was peeled off from the master mold and was bonded to a 1-inch by 3-inch glass slide following surface activation using oxygen plasma. The bonded microfluidic channel

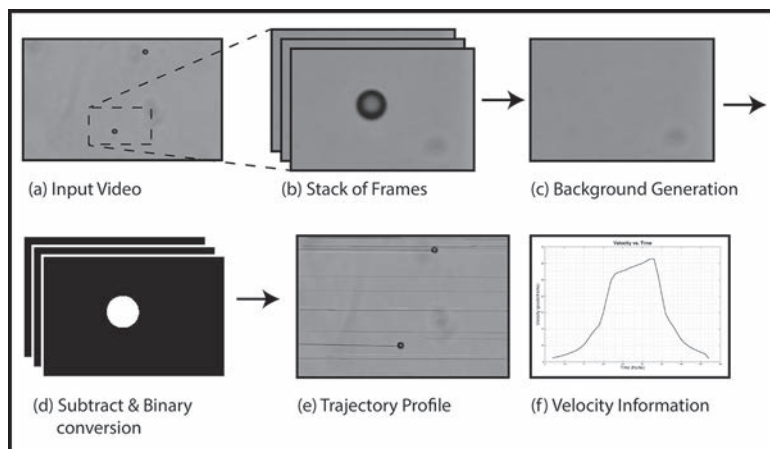


Figure 2: Schematic of developed image processing software.

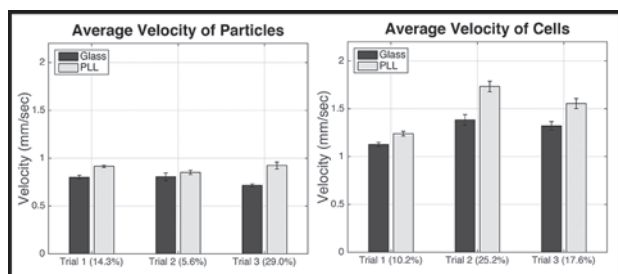


Figure 3: Velocities of particles and cells in the device. Error bars represent 95% confidence intervals of mean velocities. Values next to trial numbers represent percent change in mean velocities.

was then partially coated by flowing a 0.01% PLL solution from the outlet to cover approximately half of the channel. Following a 30 min incubation, the device was flushed thoroughly with de-ionized (DI) water from the inlet.

**Data Acquisition and Image Processing.** Using a syringe pump, cells and polymer beads (Polybead® Microspheres with 15  $\mu\text{m}$  diameter) suspended in phosphate-buffered saline (PBS) were driven through the microfluidic device from the inlet at a rate of 5  $\mu\text{L}/\text{min}$ . The cells used in the experiment were human ovarian cancer (HEY) cells. Confluent cultures of cells were trypsinized and dissociated by gentle pipetting to create single cell suspension in PBS.

A high-speed camera (Vision Research, Phantom v7.3) connected to an inverted optical microscope (Nikon Ti) was used to record the movement of the cells and particles as they flow in the uncoated and the PLL-coated region. The field of view in each video was aligned such that the measurements were taken at identical points along the width of microfluidic channel to account for the parabolic flow profile. The recorded video was analyzed using a cell-tracking program developed using MATLAB for this experiment. The program was designed to; 1) analyze the video frame by frame, 2) create a static background, and 3) perform background subtraction to find the location of

cells and particles in each frame. Using the known frame capture rate and calibrated pixel dimension, actual particle velocities were calculated (Figure 2).

### Results:

We measured the average velocities of particles and cells in repeated experiments. Overall, the polymer beads showed a 16.2% increase in mean velocity, whereas the cells showed a 17.7% increase in mean velocity when they entered the PLL-coated region (Figure 3). These results are in conflict with our initial predictions. We hypothesized that the cells should move slower on the

PLL-coated region due to the electrostatic attraction between plasma membranes and the PLL layer. Our measurements indicate higher velocities for both cells and particles over PLL-coated surface. Moreover, there is negligible difference between the cells and particles' velocities suggesting an effect independent of electrostatic interactions.

### Future Work:

Future experiments will focus on the investigation of various factors that can affect the changes in velocity of moving particles and cells. We will use surface characterization tools to analyze device surface coatings and then optimize our surface functionalization protocols. The image analysis program will be improved to increase the signal-to-noise ratios in cell and particle velocity measurements. Following the analysis of the parameters that mainly affect the motion of cells, functionalization of the channel using antibodies will be studied to study specific cell detection.

### Acknowledgements:

I would like to thank Professor Fatih Sarioglu, Ruxiu Liu, and the Georgia Tech coordinators for their assistance. This research was supported by the National Nanotechnology Infrastructure Network Research Experience for Undergraduates (NNIN REU) Program and National Science Foundation under Grant No. ECCS-0335765.

### References:

- [1] R. J. Garde. 2000. Mechanics of Sediment Transportation and Alluvial Stream Problems. 3<sup>rd</sup> ed. Delhi, India: New Age International.

# High-Throughput Drug Screening *in vivo* Using Droplet Microfluidics

**Alejandro Sanchez**

**Chemistry, University of Houston**

**NNIN REU Site: Center for Nanoscale Systems, Harvard University, Cambridge, MA**

*NNIN REU Principal Investigator: Dr. David Weitz, Applied Physics, Harvard University*

*NNIN REU Mentor: Dr. Anindita Basu, Applied Physics, Harvard University; Broad Institute of MIT and Harvard*

*Contact: alejandro.sanchez1794@gmail.com, weitz@physics.harvard.edu, abasu@broadinstitute.org*

## Introduction:

Early stages of drug screening involve a broad library of drug compounds. Oftentimes the limiting factor in initial screening is the low volumes of candidate drugs. Microliter well assays are the current conventional method for initial screening. However, a well can only efficiently pipette 10  $\mu$ L while in a droplet of 50  $\mu$ m diameter the volume is 65 pL,  $10^5$  times less than a well. The aim of this project was to develop a platform to screen chemotherapeutic drugs at different doses on cancer cell lines at high-throughput using; a) live/dead cell assay, b) fluorescent dye as indicator of drug concentration, and c) photomultiplier tubes (PMT) for readout for both drug concentrations and cell state within each droplet.

The novelty of high-throughput drug screening using droplet microfluidics has the capability of decreasing time for analysis, volumes of reagents, and cost using polydimethylsiloxane (PDMS) microfluidic technology, while increasing the number of quantified interactions in comparison to conventional drug screening. High throughput is describing the fact that in 20 minutes  $\sim 10^5$  cell and drug interaction chambers can be screened with PMT sensor technology. Droplet chambers and PMT allow us to rapidly screen for candidate drugs by quantifying their efficacy at distinct concentrations in killing cancer cells as function of time with high statistical resolution.

## Experimental Procedure:

PDMS is favored as a material for microfluidic device fabrication because it is optically transparent, biocompatible, and gas permeable, among other benefits. Device fabrication consisted of standard soft lithography methods. First, SU-8 photoresist was spun onto a silicon wafer and placed under UV. After developing with a photo-mask, it became a master mold to make PDMS devices. Photoresist was poured onto the mold and then bonded to a glass slide by plasma oxidation. Lastly the channels were coated with aquapel to make the micro-channels hydrophobic [1].

The feature size of the co-encapsulation flow device was 50  $\mu$ m, which determined the size of the droplets. It is these narrow micro-channels diameters that give laminar fluid dynamics, which are governed by low Reynolds numbers.

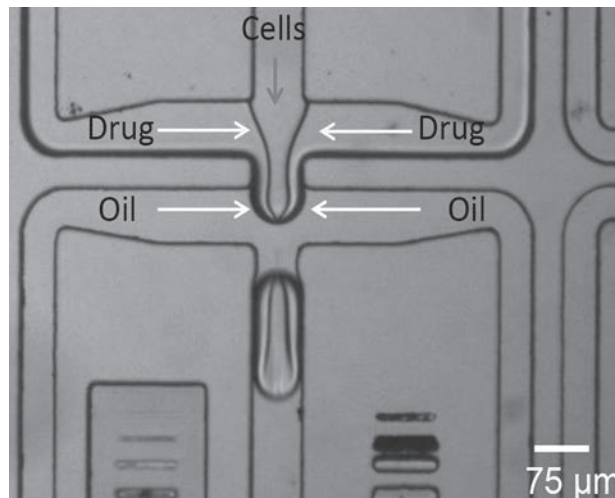


Figure 1: The junction of the co-encapsulation flow device showing formation of water-in-oil emulsions.

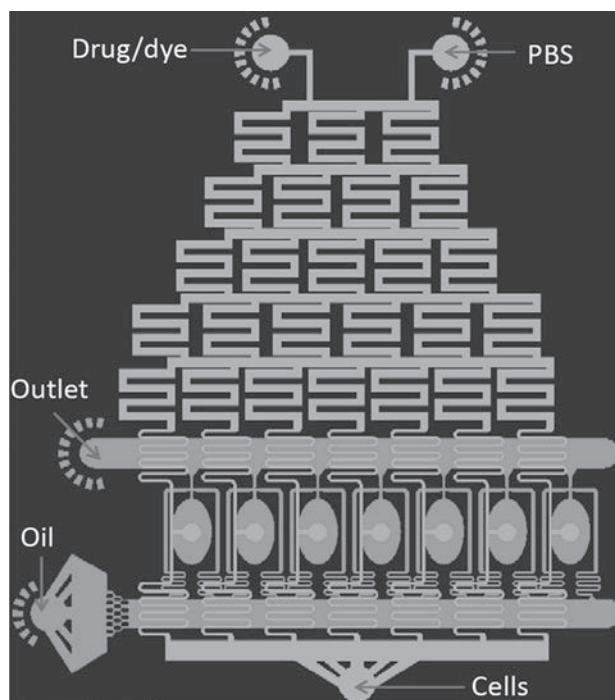


Figure 2: CAD of the bilayer PDMS microfluidic device generating droplets with varying drug concentrations.

Droplets were water-in-oil emulsions that were stabilized by a fluorinated surfactant. The aqueous media contained phosphate-buffered saline (PBS) and a hydrophilic fluorescent dye. The emulsions were formed by a continuous flow of the oil; droplet fission occurred when the continuous oil phase exerted sufficient viscous stress that caused an imbalance in the surface tension [2].

The water-in-oil emulsion occurred in a flow-focused geometry as seen in Figure 1. The manipulation of the flow rates of the PBS and dye with respect to each other determined the concentration of the dye within the droplet.

If 800  $\mu\text{L/s}$  of oil was pumped with 300  $\mu\text{L/s}$  of PBS and 100  $\mu\text{L/s}$  of dye, then you would expect the droplets to have a relative dye concentration of 25%. We strived to generate drug concentrations that would be of interest. After emulsification, there was a serpentine region in the device that promoted mixing of the droplet contents before the mixture exited the device through the outlet and was subsequently incubated.

Figure 2 shows a computer aided design (CAD) for a bilayer PDMS microfluidic device that generates a drug gradient by serial mixing in micro-channels within one layer, and another layer for creating picoliter-sized water-in-oil emulsion where the drug at different concentrations and lymphoblast cancer cells are co-encapsulated in a droplet in parallel. In the drug concentration gradient generating device, mixing is induced by the changes in velocity created by the changes in channel widths (Bernoulli's principle) and tree branching pattern. The advantage of this device is to reliably produce same size droplets with varying concentrations all at once rather than generating varying concentration droplets independently using a co-flow device.

For developmental and experimental purposes chemotherapeutic drugs and cancer lymphoma cells were not used, because the concept has already been proven. More so the focus was to improve the reproducibility of dye concentration within droplets, size of droplets, and design of the serpentine drug concentration gradient generating device.

## Results and Conclusions:

The data acquisition was driven by the PMT to identify cell state (live/dead), drug concentration in droplets, relative sizes of droplets, and presence of cell in droplet at high-throughput. A PMT heat map showed the distribution of different concentration clusters and relative sizes.

In Figure 3, there is a vertical smear indicating diffusion between the droplets. After changing surfactant and

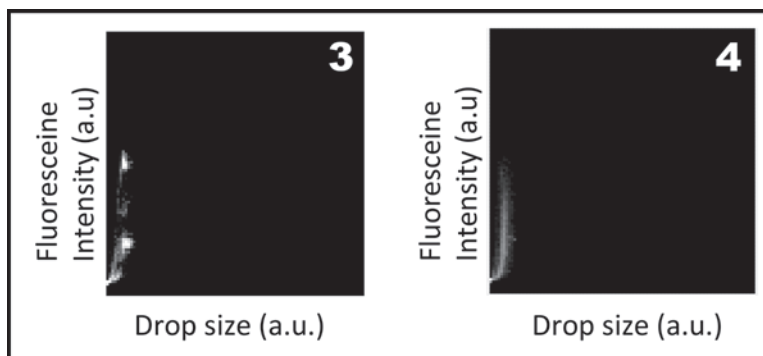


**Figure 3, left:** PMT heat map representative of same size droplets that have diffused during droplet incubation. **Figure 4, right:** PMT heat map demonstrating suppressed diffusion during droplet incubation.

adding a greater concentration of “empty” drops, diffusion was suppressed.

A horizontal smear would be indicative of droplets lacking size uniformity. As seen in Figure 4, the diffusion was suppressed successfully by having independent clusters of varying dye concentrations. Fluorescence imaging was also used to observe and quantify dye concentration in the drops, however it is labor intensive and impractical for high throughput and the reason for using PMT.

## Future Work:

Moving forward we would like to optimize flows and tree design for best mixing and reproducible concentration gradients. Using the PMT, we would like to perform time plots to observe diffusion during droplet incubation periods. Summation effects of drugs would also be interesting to observe drug synergy attacking different cell mechanisms leading to apoptosis. In addition, we would like to evaluate toxicity in healthy cells, not only drug efficacy.

## Acknowledgements:

I would like to thank God, my research mentor Dr. Anindita Basu, my principal investigator Dr. David Weitz, the National Nanotechnology Infrastructure Network Research Experience for Undergraduates (NNIN REU) Program, Dr. Randall Lee, and NSF for funding under Grant ECCS-0335765.

## References:

- [1] YC Tan, et al. Design of microfluidic channel geometries for the control of droplet volume, chemical concentration, and sorting. *Lab on a chip*, 4, 292-298, 2004.
- [2] Whitesides, G., et al. *Basic Microfluidic and Soft Lithographic Techniques. Optofluidics: Fundamentals, Devices, and Applications*, McGraw-Hill Biophotonics, 2009.

# Micropatterns and PDMS Microdevices for the Investigation of Cardiac Muscle Cell Structure and Function

**Anisa Swei**

**Biomedical Engineering, Worcester Polytechnic Institute**

**NNIN REU Site: Cornell NanoScale Science and Technology Facility, Cornell University, Ithaca, NY**

*NNIN REU Principal Investigator: Prof. Jan Lammerding, Biomedical Engineering/Weill Institute for Cell and Molecular Biology, Cornell University*

*NNIN REU Mentors: Dr. Patricia Davidson and Gregory Fedorchak, Biomedical Engineering/Weill Institute for CMB, Cornell University*

*Contact: aswei@wpi.edu, jan.lammerding@cornell.edu, patricia.davidson@cornell.edu, grf44@cornell.edu*

## Abstract and Introduction:

Heart disease is the leading cause of death in the United States, responsible for an estimated 787,000 deaths in 2011 [1]. Genetic mutations are the cause of up to one-third of cases of dilated cardiomyopathy; mutations in the gene encoding lamin A/C alone accounts for 10% of inherited cases. Lamin A/C is an important component of the nuclear envelope: these proteins are essential for many cellular functions, such as preservation of the nucleus' shape, DNA replication, regulation of transcription, and chromatin organization [2]. One hypothesis is that these mutations interfere with heart muscle cell organization and/or the exertion of contractile forces, which are essential for these cells to properly function. In this project we designed and built polydimethylsiloxane (PDMS) devices to (a) examine the organization of the cytoskeleton and (b) assess the contractile forces of healthy and lamin A/C mutant human cardiac cells. By developing these two devices for the examination of cardiac cell functions, we hope to understand the role lamin A/C has on dilated cardiomyopathy.

10 mm × 10 mm squares containing rectangles with an area of 50 μm<sup>2</sup>, but different aspect ratios, with rectangles spaced 200 μm apart. From the design, we fabricated a mask and prepared the molds for the stamps using SU-8 photolithography techniques. The resulting features on the wafer were rectangular pillars 20 μm tall. Figure 1 shows a schematic of the procedures used to produce the micropattern device.

After microfabrication, molds were fabricated using PDMS. A 50 μg/mL solution of fibronectin, an extracellular matrix protein, was incubated on the PDMS stamps for an hour. The fibronectin-coated PDMS was placed into contact with a plasma cleaned glass coverslip to print rectangular fibronectin areas. The glass coverslips were then immersed in poly(L-lysine)-graft-poly(ethylene glycol) (PLL-g-PEG), which deposited on the glass that was not covered in fibronectin and prevents cell adhesion, so that cells could only adhere to the rectangular fibronectin patterns.

The glass coverslips were prepared for tissue culture by incubating in antibiotic solution, and human fibroblasts were cultured and then observed on the microscope.

The second device consisted of flexible PDMS micropillars, ranging in sizes and center-to-center distances. As the cells exerted forces onto the pillars, the quantification of cardiac cell contractile forces could be determined from their deflections. A mask, consisting of circles with a 1 μm diameter and 2 μm pitch, was used to microfabricate the pillars using standard lithography techniques.

Hexamethyldisilazane (HMDS) and nLOF-2020 (negative photoresist) was spin-coated on a silicon wafer, which was then exposed on the Autostep, post-exposure baked and developed. The wafer was placed in the Oxford 80 and processed for oxygen descum (straightening the pillar edges) and then oxide-etched to remove the silicon wafer's native oxide. The wafer was placed in the deep reaction ion etcher to perform a Bosch process, followed by oxide stripping to remove the photoresist.

## Experiment Procedure:

The first device consisted of PDMS stamps that were used to pattern rectangular shapes of extracellular matrix proteins with various aspect ratios. The stamp design consisted of

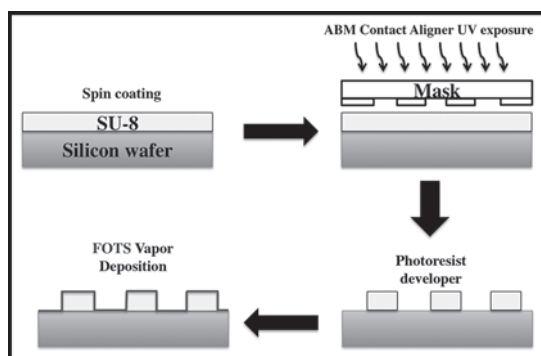


Figure 1: Overview of SU-8 photolithography used for the development of the micropattern device.

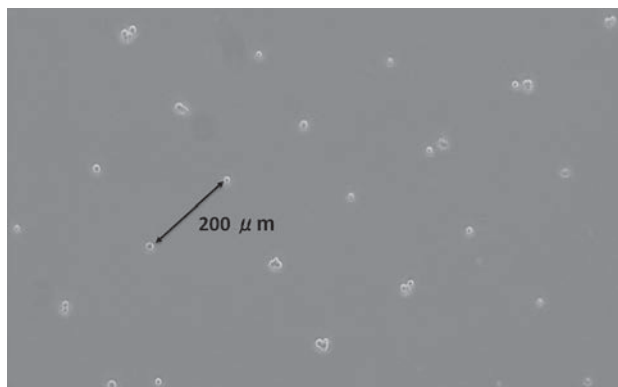


Figure 2: Bright-field contrast of the  $70 \times 35 \mu\text{m}^2$  stamp, spaced at  $200 \mu\text{m}$ , imaged at  $5\times$  objective.

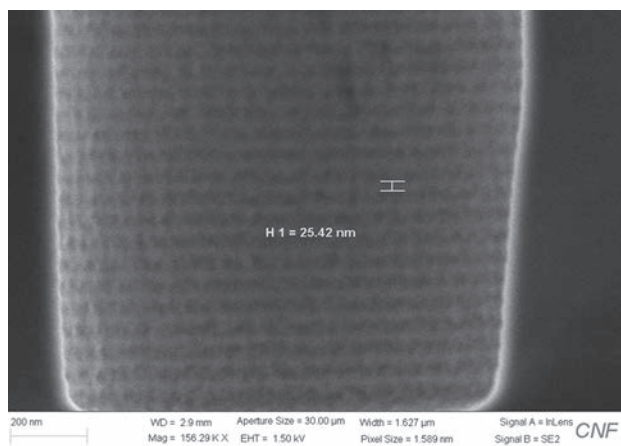


Figure 3: SEM image of the Bosch process with each scallop having a height of  $25.42 \text{ nm}$ .

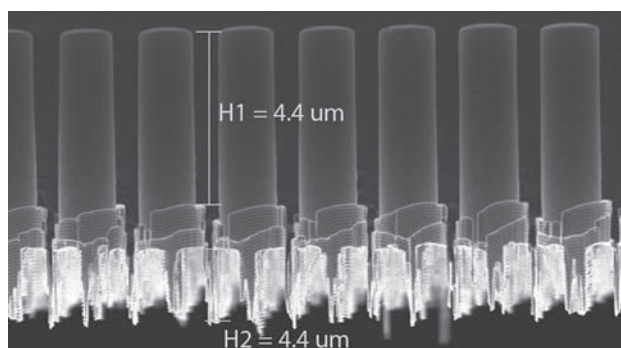


Figure 4: SEM image of the  $1 \mu\text{m}$ , with a center-to-center pitch of  $2 \mu\text{m}$ , device having a height of  $4.44 \mu\text{m}$ . (See cover!)

## Results and Conclusions:

The fabrication process for the micropattern device successfully created the desired height of  $20 \mu\text{m}$  as well as obtaining PDMS stamps from the molds. This was verified by optical microscopy, where the molds had proper shape and size. Following the microfabrication process, the preliminary studies with human fibroblasts showed

that the cells had adhered to the stamped patterns. The initial studies have shown that the application of a PDMS stamps with various patterns has the ability to control cell adhesion and placement. Figure 2 shows the bright-field contrast of cells adhering to a substrate patterned with the  $70 \times 35 \mu\text{m}^2$  stamp, where (mostly) individual cells are being spaced  $200 \mu\text{m}$  apart.

Initially, the micropillar device fabrication process had used similar SU-8 photolithography techniques as the micropattern device. However, this method resulted in cracked SU-8, as well as pillars floating off the device in the SU-8 developer. Thus, the method described in the experimental procedure was used. From the results, the device had successfully performed the Bosch process, where the pillars had scallops that were fairly linear, with an approximate scallop height of  $25 \text{ nm}$  as seen in Figure 3. However, issues arose in the deep reaction ion etcher process, causing the photoresist to burn, resulting in pillars not fully developing. Figure 4 shows that the pillar height was approximately  $4.44 \mu\text{m}$ . Unfortunately, due to the burns, the pillar height did not meet the goal of  $10 \mu\text{m}$ .

## Future Work:

The micropattern device will be used to assess variations in cytoskeletal alignment between mutated and wild-type cardiac cells. The micropillar device is being finalized for the quantification of cellular force generation, where optimizing techniques being considered include a positive photoresist, changing feature sizes and the addition of an oxide layer prior to spin-coating HMDS and photoresist.

From the initial studies conducted, the fibroblasts adhered to micropattern stamps, while cardiomyocytes contracted on PDMS pillars. Using these devices, we will be able to better understand the role of lamin mutations in dilated cardiomyopathy.

## Acknowledgements:

I acknowledge the National Nanotechnology Infrastructure Network Research Experience for Undergraduates (NNIN REU) Program, the Cornell NanoScale Science and Technology Facility, the National Science Foundation (ECCS-0335765). Thank you to the CNF staff, Christopher Martin (CNF user), Ryan Badman (CNF fellow), Jan Lammerding, and the members of the Lammerding lab.

## References:

- [1] Roger, V., et al. AHA Statistical Update. 2011.
- [2] Fox, SI. Human Physiology 13<sup>th</sup> Edition 2011. McGraw-Hill Publishing. New York, New York.

# Development of Dual-Modality Nanoparticles for PET/MR

Cyrus Thompson

Materials Science and Engineering, University of Wisconsin Madison

**NNIN REU Site: Nano Research Facility, Washington University in St. Louis, St. Louis, MO**

NNIN REU Principal Investigator: Yongjian Liu, Radiology, Washington University School of Medicine

NNIN REU Mentor: Yongfeng Zhao, Radiology, Washington University School of Medicine

Contact: crthompson3@wisc.edu, liuyo@mir.wustl.edu, zhaoyo@mir.wustl.edu

## Abstract:

Behind strong medical treatments lie accurate diagnostics that commonly involve imaging—such as magnetic resonance imaging (MRI) and positron emission tomography (PET). Recently, to overcome limitations of each individual modality, PET and MRI are combined into a more efficient and accurate procedure for functional evaluation of imaging agent uptake with high resolution anatomy. However, this new technique requires new contrast agents enabling the dual-modality assessment. To date, numerous nanoparticles have been researched, but many require chelators for conjugation of radioisotopes to the nanoparticle surface. This raises concerns of radiolabeling stability and diagnostic accuracy. To address these issues, our project aimed at developing new PET/MR dual-modality nanoparticles by doping MRI contrast agents such as iron oxide (IO) and gadolinium oxide (GdO) with positron-emitter  $^{64}\text{Cu}$ . We first focused on the synthesis of nanoparticles through one-step reduction, copper doping efficiency, size and shape uniformity, contrast magnitude, structural stability, and surface modification. We then successfully incorporated  $^{64}\text{Cu}$  into IO with ~ 30% incorporation of total radioactivity and achieved high specific activity for sensitive PET detection. Further, phantom studies and *in vivo* pharmacokinetic evaluations suggested potential applications of this particle for PET/MR. We will continue the optimization for further *in vivo* animal PET/MRI studies.

## Introduction:

With MRI we are able to achieve excellent soft tissue and soft organ contrast providing images with high anatomical accuracy. This can be helpful in locating a patient's specific medical condition such as a tumor. However, it cannot provide functional information such as tissue growth rate and metabolism. In order to collect this information a patient might have to undergo additional imaging techniques. A common approach is PET imaging, which offers the needed sensitivity through detection of extremely minute amounts of radioactive labeled agents.

When these imaging techniques are combined we then need dual-modality agents. In our research, nanoparticle systems were exploited because of their multifunctionality capability. Specifically, we combined two detection elements, radionuclides and MRI agents, but future work could involve additional components used for targeting and therapeutic payloads. Operating on the nanoscale also offers enhanced *in vivo* stability, efficacy, and reduced toxicity. With such potential it is no surprise that six nanoparticle delivery systems for cancer are already on the market and numerous others in clinical development [1].

## Experimental Procedure:

**Cu-IO Synthesis.** Iron oxide particles were synthesized following a modified one-step copper incorporation

thermal decomposition procedure [2]. To study effects of copper incorporation on particle characteristics we varied the percentage of copper in the reaction medium (0%, 2% and 10%) through addition of copper chloride dihydrate.

**Cu-GdO Synthesis.** Gadolinium oxide particles were synthesized following a modified one-step copper incorporation polyol process [3]. Similarly to IO we studied the effects of copper incorporation by varying the presence of copper in the reaction medium (0% and 5%).

**Surface Modification.** Before conducting any *in vivo* study, particle surfaces first needed to be modified for stable aqueous dispersion. This was achieved through the exchange of initial hydrophobic coatings, a product of synthesis reagents, with polyethylene glycol (PEG) through a modified PEGylation process [2]. Particles were first synthesized with non-radioactive copper and studied via transmission electron microscope (TEM) in order to characterize size and shape. Copper incorporation was then confirmed with inductively coupled plasma mass spectrometry (ICP-MS). Finally, after successful surface modification for stable aqueous dispersion the synthesis was repeated except with the use of  $^{64}\text{Cu}$ . Further studies were then conducted on structural stability via thin layer chromatography (TLC), contrast magnitude via PET and MR phantom, and pharmacokinetic properties via mouse biodistributions.

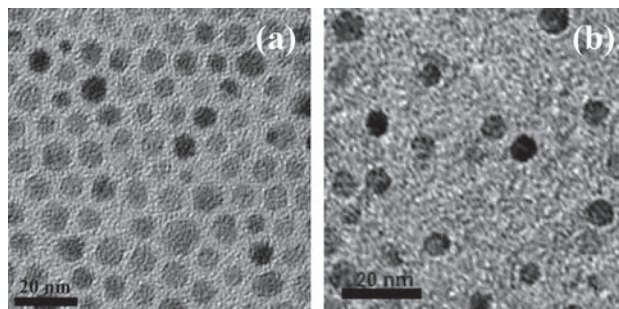


Figure 1: TEM images of (a) IO-0% Cu and (b) GdO-0% Cu with 20 nm scale bars.

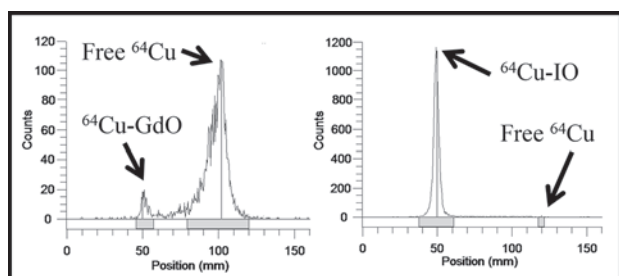


Figure 3: Radio-TLC plots showing  $^{64}\text{Cu}$  incorporation into (left) GdO and (right) IO.

## Results and Conclusions:

Synthetic procedures produced particles monodisperse in size and shape for both IO and GdO as seen in Figure 1 and 2. It can also be seen that there were only slight changes in particle diameters as the percentage of copper increased. This consistency and stability is beneficial as it allows for the variable tuning of copper incorporation without significant changes to other features such as PET and MR contrast magnitude; confirmed via phantom studies. Further, we were able to confirm the presence of copper by ICP-MS. While the actual values are lower than amounts present during synthesis we were successful nonetheless as the high sensitivity of PET is capable of detecting such minute amounts of  $^{64}\text{Cu}$ .

When particles were synthesized with  $^{64}\text{Cu}$  we measured radiolabeling stability by observing how much  $^{64}\text{Cu}$  remained intact versus how much broke free from the main particle system; seen in Figure 3. For both IO and GdO we saw that  $^{64}\text{Cu}$  remained intact, but in the case of GdO there was also detachment; signified by the “Free  $^{64}\text{Cu}$ ” peak.

Since current progress with IO showed greater radiolabeling success we then studied pharmacokinetic properties of  $^{64}\text{Cu}$ -IO via mouse biodistributions. As seen in Figure 4, particle concentration in the lungs was greater than any other organ. While this suggests a potential application for drug delivery to the lungs further studies are needed to explore the underlying mechanism behind the accumulation.

Target	Measured Cu	TEM size
IO	--	$7.0 \pm 1.2$ nm
IO-2% Cu	1.4%	$8.2 \pm 1.0$ nm
IO-10% Cu	1.8%	$9.6 \pm 1.4$ nm
GdO	--	$6.3 \pm 1.6$ nm
GdO-5% Cu	0.23%	$4.6 \pm 0.9$ nm

Figure 2: Particle diameters via TEM and measured copper percentage via ICP-MS.

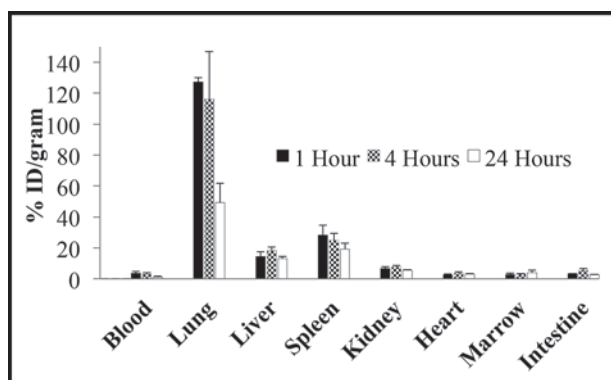


Figure 4: Mouse biodistribution study of  $^{64}\text{Cu}$ -IO.

## Future Work:

While this preliminary work was successful in using IO, GdO, and  $^{64}\text{Cu}$  for the development of dual-modality particles, we hope to increase radiolabeling incorporation and stability through synthetic procedure modifications. After optimization of both IO and GdO systems we can then continue with PET/MR imaging and exploration of *in vivo* particle accumulation.

## Acknowledgements:

I would like to thank Hannah Luehmann, Debbie Sultan, the small animal imaging facility, and  $^{64}\text{Cu}$  production team at MIR. I would also like to thank the National Nanotechnology Infrastructure Network Research Experience for Undergraduates (NNIN REU) Program and National Science Foundation for their financial support under Grant No. ECCS-0335765.

## References:

- [1] Egusquiaguirre SP, et al; *Clinical and Translational Oncology*, 14:2, 83-93 (2012).
- [2] Bridot, Jean-Luc, et al; *Journal of the American Chemical Society*, 129:16, 5076-5084 (2007).
- [3] Xie, Jin, et al; *Advanced Materials*, 19:20, 3163-3166 (2007).